DEVELOPMENTAL BIOLOGY

Alternative polyadenylation is a determinant of oncogenic Ras function

Aishwarya Subramanian[1], Mathew Hall[2], Huayun Hou[3], Marat Mufteev[1,4], Bin Yu[1], Kyoko E. Yuki[3], Haruka Nishimura[1,4], Anson Sathaseevan[1,4], Benjamin Lant[1], Beibei Zhai[5,6], James Ellis[1,4], Michael D. Wilson[3,4], Mads Daugaard[5,6], W. Brent Derry[1,4]*

Alternative polyadenylation of mRNA has important but poorly understood roles in development and cancer. Activating mutations in the Ras oncogene are common drivers of many human cancers. From a screen for enhancers of activated Ras (*let-60*) in *Caenorhabditis elegans*, we identified *cfim-1*, a subunit of the alternative polyadenylation machinery. Ablation of *cfim-1* increased penetrance of the multivulva phenotype in *let-60/Ras* gain-of-function (gf) mutants. Depletion of the human *cfim-1* ortholog *CFIm25/NUDT21* in cancer cells with KRAS mutations increased their migration and stimulated an epithelial-to-mesenchymal transition. *CFIm25*-depleted cells and *cfim-1* mutants displayed biased placement of poly(A) tails to more proximal sites in many conserved transcripts. Functional analysis of these transcripts identified the multidrug resistance protein *mrp-5/ABCC1* as a previously unidentified regulator of *C. elegans* vulva development and cell migration in human cells through alternative 3′UTR usage. Our observations demonstrate a conserved functional role for alternative polyadenylation in oncogenic Ras function.

INTRODUCTION

The transition of normal cells to the neoplastic state requires genetic alterations that include activation of oncogenes and loss of tumor suppressors. Genome-wide analysis of numerous cancers has yielded a dizzying array of secondary mutations in genes that can affect the evolution of the cancer cell and its tumorigenic potential (*1*). The Ras oncogene is conserved from yeast to human and is one of the most frequently mutated genes in cancer, with up to 30% of all tumors having gain-of-function (gf) mutations in one or more of the three Ras paralogs: *KRAS*, *HRAS*, and *NRAS* (*2*–*4*). Ras proteins are critical regulators of signaling pathways that control proliferation, cell survival, and tissue differentiation. Point mutations in the guanosine triphosphatase domain of Ras lead to constitutive activation of pro-survival pathways that contribute to tumor development and progression (*3*, *5*). Ras and other oncogenes, such as *MYC* and *NOTCH1*, require specific levels of expression, pathway activation, or cross-talk with other signaling axes to sustain tumor phenotypes in mammalian systems (*6*, *7*). Studying the mechanisms by which these signaling pathways interact is challenging using established cell lines, which are often highly mutated and aneuploid (*8*). Model organisms provide robust complementary systems to study genetic interactions within the context of living animals.

The powerful genetic tools of the nematode worm *Caenorhabditis elegans* have provided much insight into the in vivo functions of oncogenes such as Ras. Mutational activation of the *C. elegans* Ras homolog *let-60* occurs by a glycine to glutamic acid substitution at amino acid 13 (the n1046 allele), similar to the glycine to valine at amino acid 12 found in numerous human cancers. The hallmark phenotype of this *let-60* gf allele is the multivulva (Muv) phenotype, in which ectopic vulvae develop along the ventral body of the worm (*9*). Forward genetic screens in *C. elegans* have helped establish the hierarchical order of Ras/mitogen-activated protein kinase (MAPK) signaling components and uncovered numerous genes that regulate Ras/LET-60 signaling that are conserved from worm to human (*10*).

Although substantial efforts to target and directly inhibit Ras in cancer have been undertaken, these ventures have shown limited success (*11*). Likewise, strategies for targeting downstream Ras effectors have had limited clinical success due to dose-limiting toxicity of the compounds (*12*). In addition, genetic compensation and signaling cross-talk within the Ras signaling network contribute to drug resistance in many tumors (*13*). Hence, novel strategies to inhibit Ras signaling for cancer treatment are needed to overcome these obstacles. While ambitious genome sequencing efforts have uncovered variants in genes that can affect the tumorigenic state, much less is known about how epigenetic influences on gene expression and function cooperate with oncogenic pathways.

An important epigenetic mechanism of gene regulation involves an essential step in mRNA maturation, which determines the length of the 3′ untranslated region (3′UTR). This occurs by endonucleolytic cleavage of the pre-mRNA in the 3′UTR, followed by the addition of the polyadenylate [poly(A)] tail. This cleavage reaction is directed by poly(A) site (PAS) site consensus sequences composed of multiple cis elements, including (i) an AAUAAA hexamer recognized by the cleavage and polyadenylation specificity factor (CPSF) complex, (ii) downstream U/GU-rich elements that are recognized by the cleavage stimulation factor (CstF), and (iii) upstream U-rich elements recognized by cleavage factor Im (CFIm). These proteins establish a platform for subsequent recruitment of cleavage factor IIm (CFIIm) and its cofactors to form the functional 3′UTR processing holoenzyme that cleaves and polyadenylates pre-mRNA (*14*). Many genes contain multiple polyadenylation sites in their 3′UTRs, enabling cleavage and polyadenylation at different PA locations, a process termed as alternative polyadenylation (APA). APA serves to direct the placement of the poly(A) tail such that isoforms of the same gene are produced with different 3′UTR lengths. The 3′UTR contains numerous regulatory sites for the binding of microRNAs and RNA

[1]Developmental and Stem Cell Biology Program, Peter Gilgan Centre for Research and Learning, The Hospital for Sick Children, Toronto, ON M5G 0A4, Canada. [2]Department of Medicine, University of Toronto, Toronto, ON M5S 1A8, Canada. [3]Genetics and Genome Biology Program, Peter Gilgan Centre for Research and Learning, The Hospital for Sick Children, Toronto, ON M5G 0A4, Canada. [4]Department of Molecular Genetics, University of Toronto, Toronto, ON M5S 1A8, Canada. [5]Vancouver Prostate Centre, Vancouver, BC V6H 3Z6, Canada. [6]Department of Urologic Sciences, University of British Columbia, Vancouver, BC V5Z 1M9, Canada.
*Corresponding author. Email: brent.derry@sickkids.ca

binding proteins (RBPs), which regulate mRNA stability, localization, and translational efficiency (*15*).

Shorter 3′UTRs of specific genes have been associated with higher rates of proliferation, and these transcripts undergo 3′UTR lengthening as the cells reach a more differentiated state (*16*). About 30 to 40% of genes in *C. elegans* and about 70% of genes in mammals undergo APA, respectively (*17*, *18*). Alterations in APA have also been associated with tumorigenesis, where transformed cells tend to have shorter 3′UTRs of key proliferative and survival genes. This often results in higher translation rates and increased levels of proteins that promote tumorigenesis (*19*). Apart from regulating transcript stability and translation, recent studies have demonstrated how changes in APA of specific transcripts can also influence the localization and functions of resulting proteins (*20*, *21*). These observations have provided insight into the complexity of APA in diseases such as cancer; however, the precise mechanisms by which APA factors cooperate with activated oncogenes remain unknown.

In this study, we uncover evolutionarily conserved roles of the APA factor, *cfim-1/CFIm25*, in oncogenic Ras signaling using *C. elegans* and human cancer cell models. We found that *cfim-1/CFIm25* functions to buffer oncogenic Ras output by regulating the ratio of 3′UTR lengths for conserved transcripts in both systems. These include the multidrug resistance protein (*mrp-5/ABCC1*), where shortening of its 3′UTR cooperates with oncogenic Ras to enhance its functional output in development and cancer cell behavior.

RESULTS

RNAi screen uncovers *cfim-1* as a novel regulator of activated *let-60*/Ras

We previously demonstrated that the hypersensitivity to DNA damage–induced germline apoptosis of the Ras/*let-60(ga89)* gf allele, which has a more penetrant phenotype in the germ line, is dependent on a functional insulin-like growth factor 1 receptor (IGF1R) homolog, *daf-2*. Loss-of-function (lf) mutations in *daf-2* completely suppress sensitivity to DNA damage–induced germline apoptosis in *let-60(ga89)* mutants (*22*). To determine whether *daf-2* ablation also buffers activated LET-60/Ras in the soma, we turned to the vulva, the egg-laying organ of *C. elegans* that is extremely sensitive to perturbations in Ras/MAPK signaling. Loss of Ras/MAPK signaling prevents development of the vulva, resulting in the vulvaless (Vul) phenotype, whereas increased activity causes the multivulva (Muv) phenotype (*23*). The Muv phenotype used to measure hyperactive LET-60/Ras was quantified in two ways: (i) by determining the percentage of worms with at least one ectopic vulva (% Muv) and (ii) by generating a vulva induction score. Vulva induction was measured by counting the number of cells that have adopted vulval fates at the fourth larval (L4) stage (described in Materials and Methods). In normal development, only three vulval precursor cells (VPCs) adopt vulval cell fates; thus, the induction score for wild-type (WT) worms is 3.00, and the % Muv is 0 (Fig. 1, A and B). Under conditions of hyperactive LET-60/Ras, more VPCs adopted vulval cell fates, so induction scores above 3 represent Muv worms. The *let-60(n1046)* gf allele causes strong hyperactivation of Ras in somatic tissue, with an average vulval induction score of 4.09 and a penetrance of 71% Muv (Fig. 1, A to C).

The dependency on *daf-2/IGF1R* on activated LET-60/Ras was also observed in the soma, where *daf-2(lf)* suppressed the Muv phenotype of *let-60(n1046gf)* worms to 5% (Fig. 1, B and C) (*24*). This suppression was partially dependent on the transcription factor *daf-16/FOXO3a*, which functions downstream of the *daf-2/IGF1R* pathway. *daf-2(lf); let-60(gf); daf-16(null)* triple mutants had a restoration of the Muv phenotype to a 3.65 induction score and 54% Muv (Fig. 1, B and C). Details of all *C. elegans* strains are provided in Table 3. Taking advantage of the *let-60(gf); daf-2(lf)* double mutant in which the Muv phenotype was suppressed, we conducted a screen to identify novel genes that restore the Muv phenotype similar to what was observed by ablating *daf-16* (Fig. 1D).

We focused on genes that are either known or predicted to be DAF-16 transcriptional targets, reasoning that restoring the Muv phenotype in *let-60(gf)*; *daf-2(lf)* mutants would identify transcriptional targets of DAF-16 that regulate LET-60/Ras function. Therefore, a list of DAF-16 transcriptional target genes was generated from several unbiased studies, including chromatin immunoprecipitation and DNA adenine methyltransferase identification (DamID). Genes in the top 5% of methylation peaks from the DamID study and at least one other study were considered potential DAF-16 targets and prioritized for the screen (*25*–*31*). On the basis of this, we screened 202 candidate genes by RNA interference (RNAi) and found that the ablation of *cfim-1* increased the Muv phenotype of *let-60(gf)*; *daf-2(lf)* double mutants to an induction score of 3.27 and 23% Muv (Fig. 1E). This effect was even more pronounced after we generated a CRISPR deletion allele of *cfim-1* and built a *let-60(gf); daf-2(lf); cfim-1(lf)* triple mutant, which was 45% Muv and had a vulva induction score of 3.55 (Fig. 1E). *cfim-1* loss in the context of the *let-60(n1046)* single mutant (high Ras activation) did not show any additional enhancement of Muv (Fig. 1E). Since the n1046 allele is a strong *let-60*/Ras(gf) mutant, we wondered whether *cfim-1* might enhance a weaker allele. Therefore, we crossed the *cfim-1(lf)* allele into the *let-60(ga89)* mutant and observed an increase in Muv from 2 to 40%, indicating that cooperation between *cfim-1* and *let-60* was independent of the *daf-2/IGF1R* pathway (Fig. 1F). This indicates that *cfim-1(lf)* can enhance the Muv output with low levels of oncogenic Ras/LET-60 in *C. elegans* (Fig. 1G).

cfim-1 regulates APA of transcripts that mediate oncogenic *let-60*/Ras output

cfim-1 encodes the *C. elegans* homolog of mammalian *NUDT21/CFIm25*, a subunit of the 3′ polyadenylation cleavage CFIm complex that directs poly(A) tails to distal cleavage sites to produce transcripts with longer 3′UTRs. Depletion of *CFIm25* causes a global shortening in 3′UTRs, resulting in transcripts that escape negative regulation by microRNAs and/or RBPs (Fig. 2A). Therefore, we asked whether *cfim-1* modulates *let-60*/Ras signaling output through biased APA of specific transcripts. We reasoned that if *cfim-1* functions to attenuate *let-60*/Ras signaling output, then changes in the 3′UTRs of genes in *cfim-1(lf)* mutants would uncover proteins that either feed back to the Ras/MAPK pathway or amplify downstream signaling. Worms were subjected to whole-genome 3′UTR sequencing, and downstream analysis was performed by calculating the proximal poly(A) site usage (PPAU). *cfim-1(lf)* single and *daf-2(lf); cfim-1(lf)* double mutants exhibited substantial 3′UTR shortening, where a significant portion of genes had a higher number of reads mapping to the most proximal PA site ($P < 2.2 \times 10^{-16}$) (Fig. 2, B and C, and fig. S1B). In contrast, the *daf-2(lf)* single and *daf-2(lf); daf-16(lf)* double mutants did not exhibit notable alterations in their 3′UTR landscapes compared with WT controls (fig. S1, A and B). Given that *cfim-1* was initially screened as a predicted DAF-16 target, we investigated the transcript levels of *cfim-1* and found that it was not significantly

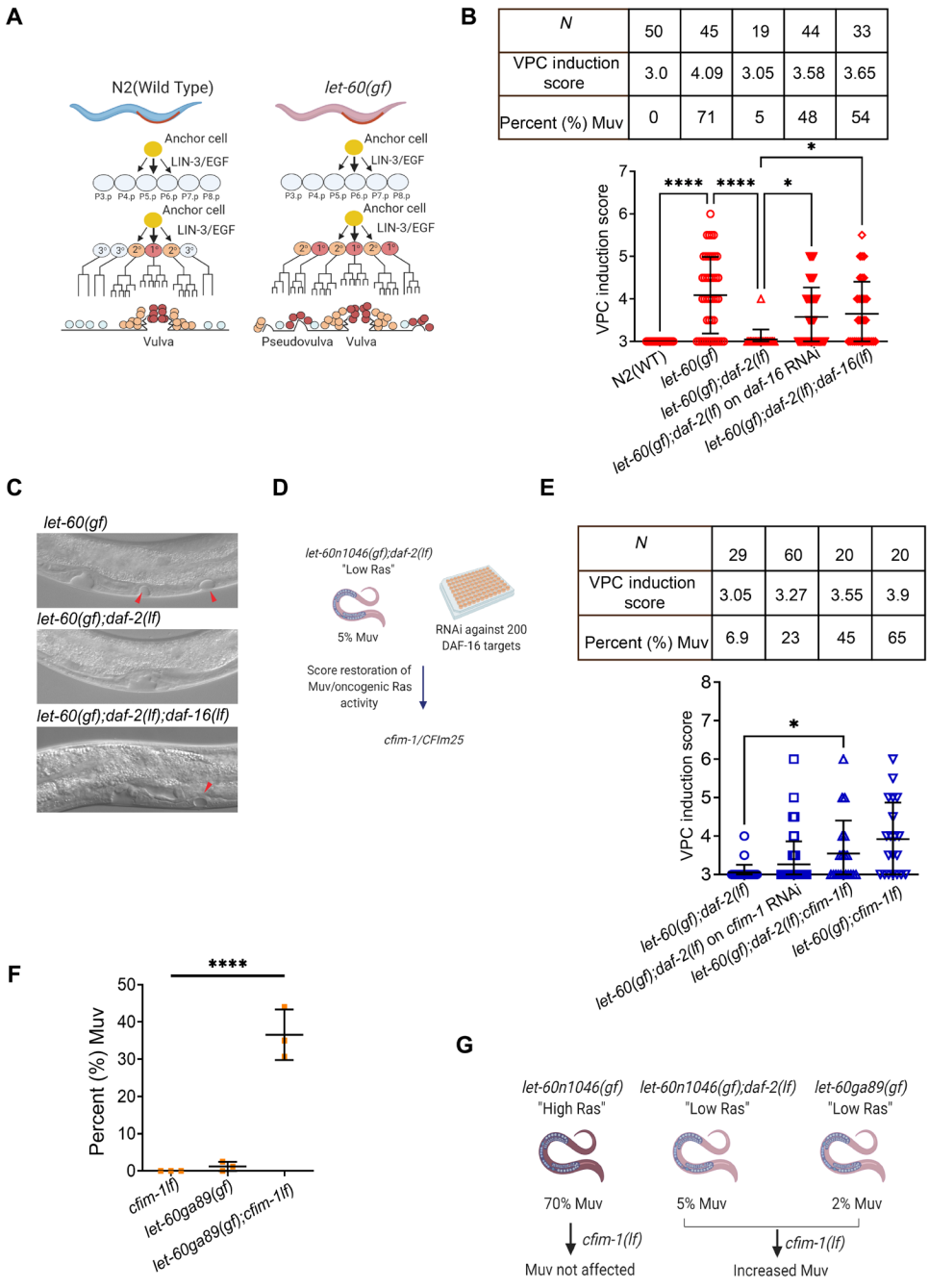

Fig. 1. *cfim-1* regulates oncogenic Ras activity in *C. elegans*. (**A**) Schematic outline of vulval development in *C. elegans*. (**B**) VPC induction scores for WT (N2) and combinations of *let-60(gf)*, *daf-2(lf)*, and *daf-16(lf)* mutants. % Muv indicates the percentage of animals with more than three VPCs induced. *N* indicates the number of animals measured. *Y*-axis origin is set to 3 to represent the normal number of VPCs that are induced to divide. ****$P < 0.0001$ and *$P < 0.05$, one-way analysis of variance (ANOVA) with Tukey's post hoc test. Detailed descriptions for all strains used in the study are described in Materials and Methods. (**C**) Representative images of larval 4 stage (L4) worms expressing the hyperactive *let-60(n1046)* allele; *let-60(gf)*; *daf-2(lf)* double mutant, in which the Muv phenotype was completely suppressed; and *let-60(gf); daf-2(lf); daf-16(lf)* triple mutant, in which the Muv phenotype was partially restored. Red arrows denote ectopic pseudovulvae. (**D**) Schematic representation of screen performed by feeding *let-60(gf); daf-2(lf)* worms (suppressed Muv) RNAi against DAF-16 target genes. (**E**) VPC induction scores for *let-60(gf); daf-2(lf)* on HT115 control and *cfim-1* RNAi, *let-60(gf); daf-2(lf); cfim-1(lf)* mutants, and *let-60(gf); cfim-1(lf)* mutants. % Muv indicates the percentage of animals with more than three VPCs induced. *N* indicates the number of animals measured. *Y*-axis origin is set to 3 to represent the normal number of VPCs that are induced to divide. *$P < 0.05$, one-way ANOVA with Tukey's post hoc test. (**F**) Percentage (%) Muv scored for the *let-60(ga89gf)* and *let-60(ga89gf); cfim-1(lf)* mutants. Each data point represents quantification from three independent experiments. ****$P < 0.0001$, one-way ANOVA with Tukey's post hoc test compared to *cfim-1(lf)* or *let-60(ga89)*. (**G**) Schematic representation of the effect of *cfim-1* loss in the context of different levels of Ras activation.

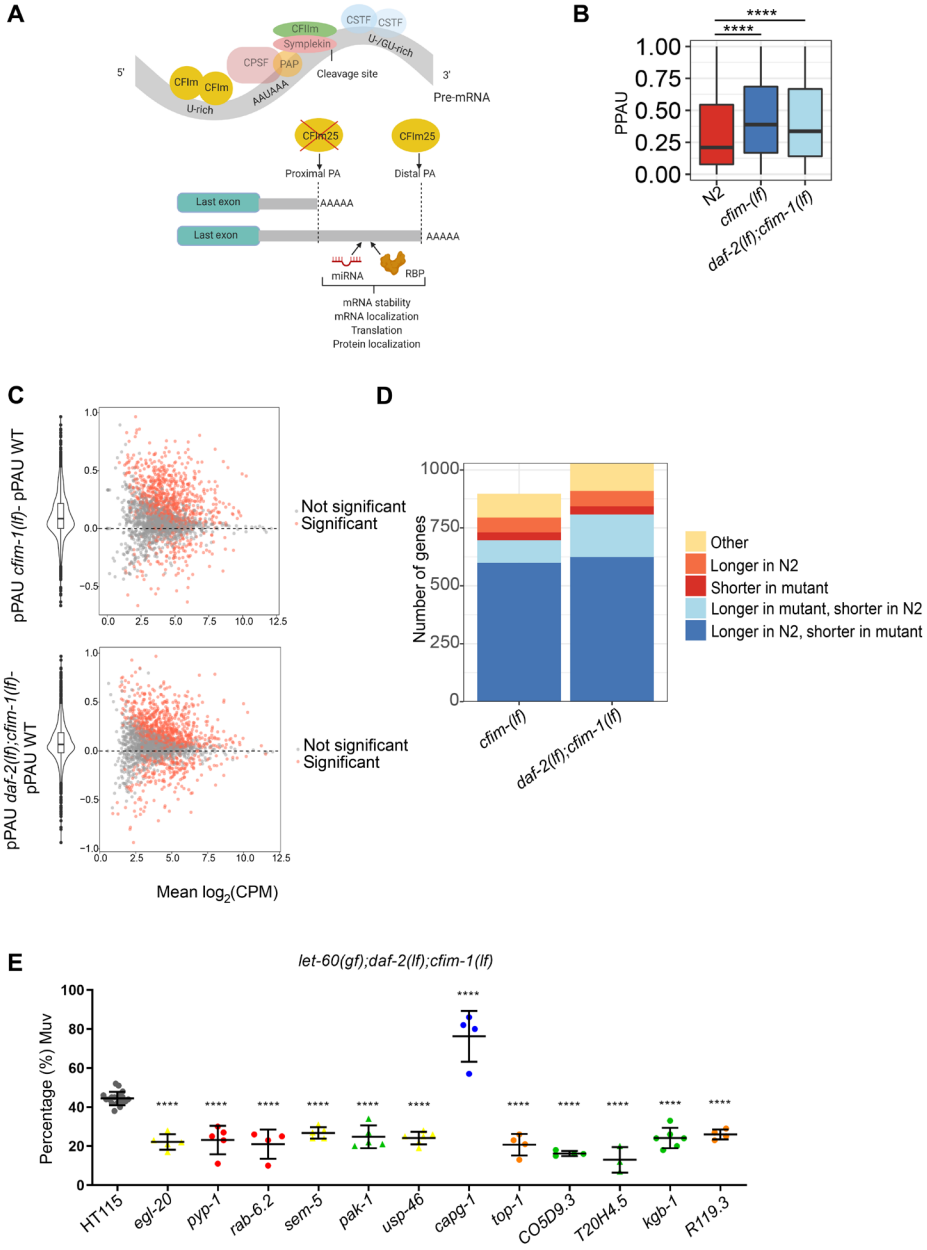

Fig. 2. *cfim-1* loss promotes 3′UTR shortening of *let-60*/Ras pathway–related transcripts. (**A**) Schematic outline of CFIM-1/CFIm25 function in the context of APA. CFIm25 is a component of the CFIm complex (denoted in yellow), which, together with other protein complexes, dictates polyadenylation of transcripts. CFIm25 biases toward the usage of distal polyadenylation sites, resulting in a longer 3′UTR. The longer 3′UTR often contains regulatory sequences such as microRNA (miRNA) and RBP sites, which regulates transcript stability and translation. Loss of CFIm25 is associated with shortening of 3′UTRs and subsequent loss of regulatory sequences. (**B**) Proximal polyadenylation site usage (PPAU) calculated in *cfim-1(lf)* and *daf-2(lf); cfim-1(lf)* strains. ****$P < 2.2 \times 10^{-16}$ compared with N2 controls. Data are the average from three independent replicates for each strain. (**C**) Scatter diagram showing the distribution of APA-regulated genes based on delta-PPAU of respective mutants versus expression. A higher/positive PPAU indicates that a proximal PA site is selected for that gene and vice versa. A significant proportion of genes show positive delta-PPAU, indicating increased usage of the proximal polyadenylation site in *cfim-1(lf)* and *daf-2(lf); cfim-1(lf)* mutants. Red dots represent genes with significant PPAU, and gray is nonsignificant. Violin plot shows the distribution of genes based on PPAU calculation in each strain. CPM, counts per million. (**D**) DEXSeq analysis and quantification of the number of genes altered by APA. "Shorter" and "longer" denote the increased expression of this isoform in the respective strains as described in fig. S2. (**E**) RNAi screen of the Ras pathway–associated genes in the *let-60(gf); daf-2(lf); cfim-1(lf)* mutant. Each data point represents an independent experiment. Colors/shapes of data points correlate with the indicated colors/shapes of genes (representing functional categories) in network analysis (fig. S3).

altered in *daf-2(lf)* and *daf-2(lf); daf-16(lf)* strains compared to the known DAF-16 targets, indicating that *cfim-1* is not likely a transcriptional target of DAF-16 (fig. S1C). These data, together with *cfim-1(lf)* restoring Muv in the *let-60(ga89)* strain, independent of *daf-2*/*IGF1R*, suggest that *cfim-1* functions downstream, or in a parallel pathway, to attenuate activated LET-60/Ras output.

We next asked how the altered 3′UTR landscape in the absence of *cfim-1* might modulate Muv in the *let-60(gf)* mutant. In addition

to measuring PPAU, we also used the DEXSeq method to classify APA events. PA sites within 3′UTR of a gene were denoted as "exons," and the number of reads mapping to these PA sites was quantified. This enabled us to classify genes into different APA classes, such as isoform switching (increase in short and decrease in long or vice versa), or changes in just one isoform (short/long), between *cfim-1(lf)* mutants compared to WT controls (fig. S2). Consistent with the UTR index results, loss of *cfim-1* significantly altered the APA landscape (Fig. 2D). We identified 505 genes with increased expression of the short isoform in both *cfim-1(lf)* single and *daf-2(lf); cfim-1(lf)* double mutants (denoted as "shorter in mutants") and 181 genes shortened specifically in the *daf-2(lf); cfim-1(lf)* double mutant (Fig. 2D). We also found that 49 genes showed a decrease in expression of the long isoform in *cfim-1(lf)* mutants. These observations are consistent with the established roles of CFIm25 in biasing toward distal PAS usage efficiency, as described in other systems (*32*, *33*). Gene Ontology analysis of the 686 genes with increased proximal PAS usage identified 119 that were enriched in Ras signaling or processes that regulate oncogenesis in mammalian cells, such as cell migration, cell cycle, and cytoskeletal dynamics, as well as genes involved in vulva development and kinase activity (fig. S3). Therefore, we screened these 119 genes by RNAi in *let-60(gf)*; *daf-2(lf)*; *cfim-1(lf)* triple mutants (45% Muv) and found 12 that modulated the Muv phenotype, of which 3 function in cell migration (*kgb-1/MAPK10*, *sem-5/GRB2*, and *pak-1/PAK1*) and 1 in vulva development (*usp-46/USP46*). Ablation of *capg-1*, a condensin complex subunit, increased the percentage of Muv (Fig. 2E). We also investigated these 12 genes in the *let-60(n1046)* single mutant and found no significant effect on the Muv phenotype, suggesting that these genes likely had *cfim-1(lf)* dependency (fig. S4A).

We further assessed the correlation between 3′UTR shortening and gene expression of the 12 *cfim-1*–dependent genes. Only *egl-20* showed increased expression with 3′UTR shortening in *daf-2(lf); cfim-1(lf)* double mutants, whereas expression of the other 11 genes did not exhibit a significant correlation (fig. S4B). This suggests that 3′UTR shortening of those genes could have other consequences, such as altered stability of specific isoforms, altered translation and localization, and function (*34*). Recently, PAK1, the human ortholog of *pak-1*, was reported to undergo APA and served as a predictive marker of glioblastoma progression (*35*). Thus, our results indicate that *cfim-1* regulates APA of common transcripts that affect oncogenic *let-60/RAS* output in *C. elegans* and human with established roles in cancer biology (Table 1).

CFIm25 regulates migration and invasion of KRAS-mutant cancer cells

To determine whether our observations in *C. elegans* were functionally conserved, we assessed *CFIm25* function in human KRAS-mutant cancer cells. We used two HCT116 isogenic cancer cell lines, where the parental line had a heterozygous KRAS G13D mutation (KRAS G13D), and its isogenic counterpart had the mutant KRAS allele knocked out (KRAS WT) (*36*). Using these cell lines, we explored the mechanism by which CFIm25 functions in the context of mutant Ras in human cancer cells.

Table 1. Disease-relevant *C. elegans* genes.

C. elegans gene	Human ortholog	Function
egl-20	*WNT16*	Cell fate regulator, paracrine signaling to promote tumor cell survival (*66*)
top-1	*TOP1*, *TOP1MT*	DNA topoisomerase, regulates DNA topology during transcription
C05D9.3	*ITGB4*	Transmembrane glycoprotein receptors that regulate cell-cell adhesion, up-regulated in many cancers (*67*)
usp-46	*USP12*, *USP46*	Deubiquitinating enzyme, has both oncogenic and tumor suppressor roles (*68*)
kgb-1	*MAPK10/JNK3*	Kinase involved in proliferation, differentiation, and cell death, activated by inflammatory cytokines (*69*)
T20H4.5	*NDUFS8*	Complex I of respiratory chain, responsible for NADH oxidation
pyp-1	*PPA1*, *PPA2*	Inorganic pyrophosphatase that plays a role in energy metabolism, up-regulated in numerous cancers (*70*)
rab-6.2	*RAB6A*	Involved in the transport of proteins from Golgi body to endoplasmic reticulum (*71*)
sem-5	*GRB2*	Activates RAS/MAPK downstream of the EGFR receptor (*72*)
R119.3	*DHRS2*	Member of the short-chain dehydrogenases family, metabolizes steroid hormones and lipids
pak-1	*PAK1*	Kinase involved in cytoskeletal remodeling, contributes to metastasis of many cancers (*73*)
capg-1	*NCAPG*	Part of the condensin complex, which condenses chromosomes during mitosis and meiosis

Ablation of *CFIm25* by small interfering RNAs (siRNAs) resulted in spindle-like morphology and cytoplasmic protrusions in cells (fig. S5A). This was reminiscent of cells undergoing an epithelial-to-mesenchymal transition (EMT), which is associated with metastatic characteristics such as increased migration and invasion. Depletion of CFIm25 significantly increased the migratory and invasive properties of KRAS G13D cells (Fig. 3A). Compared to KRAS G13D cells, KRAS WT cells showed reduced migration and invasion,

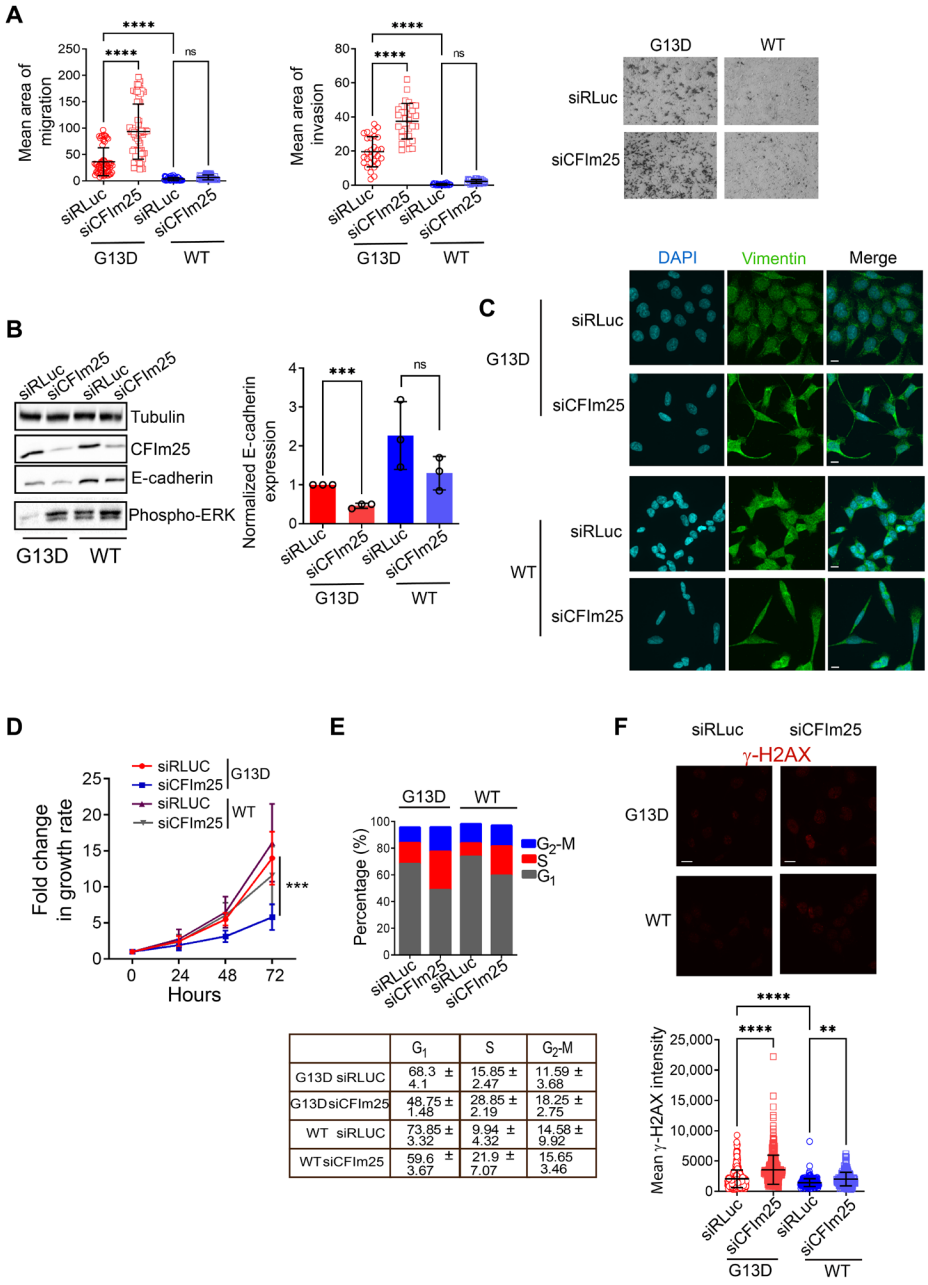

	G_1	S	G_2-M
G13D siRLUC	68.3 ± 4.1	15.85 ± 2.47	11.59 ± 3.68
G13D siCFIm25	48.75 ± 1.48	28.85 ± 2.19	18.25 ± 2.75
WT siRLUC	73.85 ± 3.32	9.94 ± 4.32	14.58 ± 9.92
WT siCFIm25	59.6 ± 3.67	21.9 ± 7.07	15.65 3.46

Fig. 3. CFIm25 depletion increases migration and invasion of KRAS-mutant cells. (**A**) Quantification of migration and invasion of KRAS G13D and KRAS WT HCT116 cell lines with/without CFIm25 KD. Each data point represents a field of view captured across three independent (migration) or two (invasion) independent experiments. ****$P < 0.0001$; ns, not significant; two-way ANOVA with Tukey's post hoc test. Representative images show a single field of view of cell migration following knockdowns with indicated siRNAs. (**B**) Representative Western blot of E-cadherin and phospho-ERK expression in KRAS WT and KRAS G13D cell lines 72 hours after transfection with the indicated siRNAs and quantification of E-cadherin protein levels normalized to tubulin across three independent experiments. (**C**) Representative immunofluorescent images (maximum projection) of Vimentin (green) in KRAS G13D and KRAS WT 72 hours after transfection with the indicated siRNAs. Nuclei were stained with DAPI (blue). Scale bars, 10 μm. (**D**) Time course growth assay measuring the growth of KRAS G13D and KRAS WT with or without CFIm25 KD using Alamar Blue. $n = 5$ independent experiments, means ± SD. ***$P < 0.001$, unpaired Student's t test. (**E**) Cell cycle analysis of KRAS G13D and KRAS WT with or without CFIm25 after 72 hours of KD. Table depicts the proportion of cells in each phase ± SD across two independent experiments. (**F**) Representative images (maximum projection) and quantification of γ-H2AX intensities in G13D and WT cells transfected with indicated siRNAs. ****$P < 0.0001$ and **$P < 0.01$, two-way ANOVA with Tukey's post hoc test. Scale bars, 14 μm.

and depletion of CFIm25 in KRAS WT cells did not significantly alter their migratory or invasive potential (Fig. 3A). We corroborated the EMT phenotype using markers and observed a decrease in the epithelial marker E-cadherin and an increase in expression of the mesenchymal marker Vimentin under CFIm25 knockdown (KD) conditions for KRAS G13D cells, with a less pronounced effect in WT cells (Fig. 3, B and C). To assess whether CFIm25 depletion can affect the MAPK pathway downstream of Ras, we assessed expression levels of phospho–extracellular signal–regulated kinase (ERK) and observed that CFIm25 depletion increased phospho-ERK levels in G13D cells (Fig. 3B). We observed higher levels of basal phospho-ERK levels in WT cells compared to G13D, and we saw slight increases with CFIm25 depletion. This observation could be attributed to feedback mechanisms as seen in prior studies (*37*). Nevertheless, CFIm25 depletion enhances RAS/MAPK signaling in cells having oncogenic Ras.

Activation of the EMT program, apart from being associated with increased cell migration and invasion, has also been associated with decreased cell proliferation (*38*). Cell growth and cell cycle analysis revealed that depletion of CFIm25 in KRAS G13D cells led to decreased cell growth and an increased fraction of cells in the S and G_2-M phases, with similar changes occurring in KRAS WT cells (Fig. 3, D and E). Oncogenic Ras activation has also been associated with increased genome instability through the accumulation of DNA damage and subsequent cell growth arrest (*39*). Since the depletion of CFIm25 induced arrest in S phase, we wondered whether this was associated with increased DNA damage. Therefore, we quantified the DNA damage marker γ-H2AX and found that CFIm25-depleted KRAS G13D cells had significantly increased levels (Fig. 3F). WT cells displayed significantly lower levels of basal γ-H2AX compared to G13D cells. CFIm25 depletion in WT cells increased γ-H2AX levels to basal levels observed in G13D cells (Fig. 3F). Thus, our observations cumulatively suggest that cells depleted of CFIm25 can undergo numerous alterations in behavior associated with the EMT program, but the presence of mutant KRAS is required for their increased migration and invasion.

We extended our studies to other KRAS-mutated cell lines to determine whether CFIm25 depletion can enhance Ras-dependent cell migration in different cell models. We made use of the DLD-1 isogenic paired cell line (KRAS G13D mutation and its WT counterpart) and three pancreatic cancer lines [BXPC3 (KRAS WT), CFPAC-I (KRAS G12V), and HPAF-II (KRAS G12D)] (*40*). Consistent with our observations in HCT116 cells, CFIm25 KD increased migration of KRAS-mutant DLD-1 with no significant effects on the WT line, as well as in the CFPAC-I and HPAF-II lines, with no significant effects observed in the KRAS WT BXPC3 cell line (fig. S5, B and C). Together, these data indicate that CFIm25 depletion has a common role in regulating EMT and cell migration in Ras-driven cancer cells.

CFIm25 regulates 3′UTR shortening of conserved genes

To identify transcripts regulated by CFIm25 in cancer cells, we subjected both KRAS-mutant and WT HCT116 cell lines, with and without CFIm25 KD, to RNA sequencing (RNA-seq) (Fig. 4A). Sequencing was performed at high depth, and we used the quantification of alternative polyadenylation (QAPA) pipeline to quantify the relative abundance of short and long 3′UTR isoforms (*41*). CFIm25 depletion significantly increased the overall PPAU in both G13D and WT cells (Fig. 4, B and C). APA event classification was performed similar to our analysis of the *C. elegans* dataset (fig. S2). From this analysis, 415 genes had increased expression of shortened isoforms, and 1369 genes also showed a decrease in long isoform expression in CFIm25 KD cells compared to controls. The APA landscape of KRAS WT cells revealed that CFIm25 depletion promoted increased proximal isoform expression of 421 genes and decreased expression of long isoforms for 1508 genes (Fig. 4D). This analysis also uncovered previously identified CFIm25 targets such as *cyclin D1* that are subject to 3′UTR shortening after CFIm25 depletion (fig. S6A), thereby validating our pipeline (*33*).

Ingenuity Pathway Analysis (IPA) of shortened transcripts in KRAS G13D cells revealed enrichment in cancer-related signaling pathways, such as protein kinase A, WNT/β-catenin, and ERK/MAPK axes, supporting our observations that CFIm25 depletion biases APA to shorter isoforms of genes involved in cancer cell migration and invasion-related pathways (fig. S6B). Mining our RNA-seq dataset also revealed expression changes in EMT-related genes after CFIm25 depletion, especially in the KRAS-mutant cells, including reduced *Occludin*, and up-regulation of multiple EMT-associated chemokines (fig. S6C), providing more evidence that CFIm25 regulates EMT (*42*).

Having identified hundreds of genes that are subject to 3′UTR shortening, we referred to the *C. elegans* APA dataset to identify novel APA-regulated genes that are important for oncogenic Ras function in human cancer cells. Since there is a high degree of pathway conservation, we reasoned that comparing the *C. elegans* and human datasets would allow us to identify key pathways subject to APA regulation. Our initial screen of genes with shortened 3′UTRs in *C. elegans* uncovered 11 that were required for enhanced Ras output (Muv) in *cfim-1(lf)* mutants. The 686 *C. elegans* genes that showed increased expression of the short/proximal isoform were converted to their corresponding human orthologs using Ortholist 2 (Fig. 4E) (*43*). This generated a list of 1215 human genes (a single *C. elegans* gene can have multiple orthologs in humans). IPA analysis of these genes showed enrichment of similar cancer-related pathways as the human shortened gene set (fig. S7A). Comparing the *C. elegans* list to the human dataset revealed 33 *C. elegans* genes that had 45 orthologous human counterparts (Fig. 4E and Table 2), including the genes that suppressed Muv such as *pak-1/PAK1*, as well as several genes that did not fall into the functional categories we initially focused on. We also compared the genes that showed decreased distal/long isoform usage and found less overlap in this case (17 genes commonly regulated) between the two organisms (fig. S7B). We therefore focused on the genes that showed increased proximal isoform expression due to the greater degree of overlap.

Ablation of the 33 *C. elegans* genes in *let-60(gf)*; *daf-2(lf)*; *cfim-1(lf)* triple mutants identified 4 genes that suppressed and 2 genes that enhanced the Muv phenotype. In addition to *pak-1/PAK1* (observed in our initial screen; Fig. 2E), other genes that suppressed the Muv phenotype were *mrp-5/ABCC*, *hst-1/NDST1*, and *mml-1/MLXIP* (Fig. 4F), which have established prosurvival or chemoresistance roles in cancers (*44*–*46*). In line with a previous study, we also observed that *daf-18/PTEN* is subject to APA regulation in both systems, and its ablation enhanced the Muv phenotype of *let-60(gf)*; *daf-2(lf)*; *cfim-1(lf)* triple mutants (Fig. 4F) (*47*). In summary, these results indicate that *cfim-1*/CFIm25 plays important and conserved roles in regulating 3′UTRs of genes that modulate Ras signaling.

ABCC1 contributes to CFIm25-dependent cell migration and EMT

One of the top candidates from our screen of the 33 *cfim-1*–regulated genes was *mrp-5*, which is orthologous to the ABCC family of

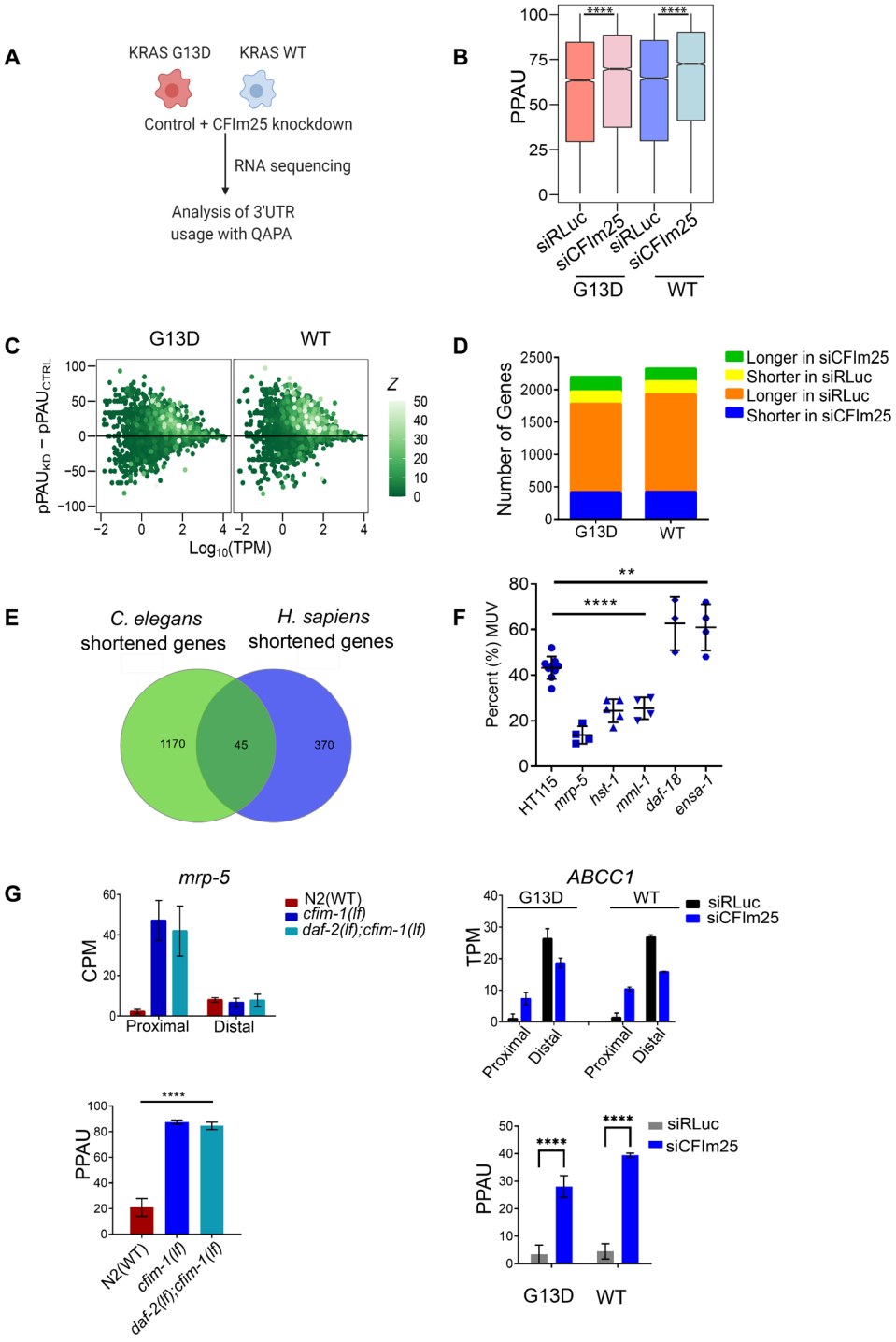

Fig. 4. *cfim-1/CFIm25* regulates 3′UTR shortening of conserved genes in *C. elegans* and human. (**A**) Schematic outline of RNA-seq performed in KRAS G13D and KRAS WT HCT116 cells. Sequencing was performed with three independent replicates for each condition. (**B**) Proximal PA site usage (PPAU) calculated for G13D and WT cells transfected with control or CFIm25 siRNA. ****$P < 0.0001$, unpaired Student's t test compared to respective controls for each cell line. Data are the average from three independent replicates for each condition. (**C**) Scatter diagram showing the distribution of APA-regulated genes based on delta-PPAU of CFIm25 KD versus control. A significant proportion of genes with high Z scores (quantification is described in Materials and Methods) show positive delta-PPAU, indicating increased usage of the proximal polyadenylation site. (**D**) Classification of APA-regulated genes into categories based on changes in isoform usage. (**E**) Venn diagram showing overlap in the number of genes with increased expression of proximal isoform in *C. elegans* (genes have been converted into their respective human orthologs) and in *H. sapiens* G13D cells. (**F**) RNAi screen of commonly regulated *C. elegans* genes in the *let-60(gf); daf-2(lf); cfim-1(lf)* triple mutants. Each data point represents quantification from an independent experiment. ****$P < 0.001$; **$P < 0.01$, unpaired Student's t test. (**G**) Bar diagrams depicting expression data for the proximal and distal isoforms of *mrp-5* and its human ortholog *ABCC1* in the indicated strains/cell lines. PPAU values across the three independent experiments are also shown. ****$P < 0.0001$, unpaired Student's t test.

Table 2. Genes that are commonly regulated by 3′UTR shortening in *C. elegans* and human cancer cells.

C. elegans genes	*H. sapiens* genes
mrp-5	*ABCC1*
mrp-5	*ABCC2*
mrp-5	*ABCC5*
F59C12.3	*AMOTL2*
ensa-1	*ARPP19*
chd-3	*CHD4*
mup-4	*COL12A1*
let-2	*COL5A1*
scpl-1	*CTDSP2*
scpl-1	*CTDSPL*
dyn-1	*DNM1*
ensa-1	*ENSA*
epc-1	*EPC2*
epn-1	*EPN3*
D1069.3	*FAM126B*
fln-2	*FLNB*
act-2	*GLIS3*
hil-1	*H1F0*
lsy-13	*ING4*
wwp-1	*ITCH*
C28H8.4	*KDELR1*
ldb-1	*LDB2*
F58A3.1	*LEMD3*
oga-1	*MGEA5*
ZK1240.3	*MID1*
mml-1	*MLXIP*
hst-1	*NDST1*
mup-4	*NOTCH2*
pak-1	*PAK1*
ceh-18	*POU2F1*
ceh-18	*POU2F2*
kin-1	*PRKACB*
pkc-3	*PRKCI*
daf-18	*PTEN*
F35G2.1	*QSOX2*
rnh-1.0	*RNASEH1*
sec-24.2	*SEC24B*
ant-1.1	*SLC25A5*
ZK1240.3	*TRIM17*
ZK1240.3	*TRIM22*
ZK1240.3	*TRIM25*
ZK1240.3	*TRIM38*
ttyh-1	*TTYH3*
ftt-2	*YWHAB*
ftt-2	*YWHAG*

transporters in humans. Multiple family members (*ABCC1*, *ABCC2*, and *ABCC5*) were observed to undergo 3′UTR shortening after CFIm25 depletion in human cancer cells (Fig. 4G and fig. S7C). Since we observed increased expression of proximal isoforms for these transporters in both *C. elegans* and human cells, we next asked whether this is functionally relevant in the context of oncogenic Ras.

To corroborate our observations in Fig. 4F, we depleted *mrp-5* in *C. elegans let-60(gf); daf-2(lf); cfim-1(lf)* triple mutants and found that it significantly suppressed VPC induction scores from 3.47 to 3.07 (Fig. 5A). Similarly, cosuppression of *ABCC1* with *CFIm25* showed the strongest suppression of migration of HCT116 G13D cells, compared with depletion of *ABCC2* and *ABCC5*. KD of *ABCC1* alone exhibited only subtle effects on cell migration (Fig. 5B and fig. S7D). Codepletion of CFIm25 and ABCC1 also increased E-cadherin levels significantly and partially decreased phospho-ERK levels, indicating that ABCC1 and CFIm25 cooperate in regulating the Ras pathway and EMT (Fig. 5C). We also found that the codepletion of CFIm25 and ABCC1 reversed the cell cycle arrest phenotype, accumulation of γ-H2AX, and partially restored cell growth rate (Fig. 5, D to F). Depletion of ABCC1 alone had only modest effects on cell cycle progression and cell growth. Thus, ABCC1 is a potent effector of cellular behavior when the APA landscape is shifted in response to CFIm25 depletion. We also assessed the functional relevance of ABCC1 and CFIm25 in DLD-1 G13D cells and found that their codepletion also reversed the increased cell migration observed with CFIm25 depletion alone (fig. S7E), indicating that CFIm25 and ABCC1 have broader roles in the context of Ras biology.

Since ABCC1 has well-known roles in drug efflux, we asked whether CFIm25-dependent regulation of ABCC1 has any effect on resistance to chemotherapeutics. Since depletion of CFIm25 causes accumulation of cells in S phase, we chose to assess the response to topoisomerase poisons that act in this phase of the cell cycle. Depletion of CFIm25 in HCT116 cells caused increased resistance to the topoisomerase inhibitor etoposide compared with controls. Codepletion of CFIm25 and ABCC1 restored sensitivity to etoposide back to control levels (Fig. 5, G to I). In contrast, we did not observe significant effects with another topoisomerase inhibitor, Camptothecin (fig. S7F). This could indicate specific dependencies displayed by CFIm25-depleted cells in response to different chemotherapeutics.

Collectively, these results show that increased expression of the short *mrp-5/ABCC1* isoform in response to CFIM-1/CFIm25 depletion is functionally important and can regulate vulva development in *C. elegans* and cancer cell behavior in the context of oncogenic Ras. Although *ABCC1* also underwent 3′UTR shortening in CFIm25-depleted KRAS WT cells, these cells did not exhibit increased migratory properties, indicating that CFIm25-dependent APA of transcripts such as *ABCC1* cooperates specifically with cellular alterations induced by oncogenic KRAS.

ABCC1 cooperates with TGFB2 signaling to regulate cell migration

Given that ABCC1 can regulate cell migration, we sought to uncover the pathways that cooperate with ABCC1 function. We surveyed our RNA-seq dataset for gene expression changes in EMT-related pathways and found that several members of the TGFB (Transforming growth factor beta) pathway were altered after CFIm25 KD. These included the TGF ligands *TGFB2*, *GDF5*, and *GDF15*, as well as the downstream effector of the TGFB pathway, *SMAD3* (Fig. 6A). We therefore asked

whether CFIm25-depleted cells were dependent on TGFB signaling for cell migration. Treating CFIM25-depleted cells with A83-01, an inhibitor of the TGFB receptor, significantly reduced cell migration (Fig. 6B). We then asked whether CFIm25 and ABCC1 can cooperate with TGFB signaling and assessed the expression of the TGFB ligands *TGFB1* and *TGFB2* under CFIm25 KD and CFIm25/ABCC1 double-KD conditions. Quantitative reverse transcription polymerase chain reaction (qRT-PCR) analysis revealed that *TGFB2*, but not *TGFB1*, was up-regulated in both CFIm25 and CFIm25/ABCC1 codepleted cells despite the dual inhibition of CFIm25 and ABCC1 causing reduced cell migration (Fig. 6C). TGFB ligands function in an autocrine or paracrine manner to influence alterations in cellular behavior through the SMAD transcription factors (*48*). Phosphorylated SMADS localize to the nucleus where they can activate the transcription of target genes involved in a wide array of cellular processes, including cell migration. We therefore assessed the expression of the downstream effectors of the pathway, SMAD2 and SMAD3. Cells were stained with a SMAD2/3 antibody, and consistent with our gene expression data, CFIm25-depleted cells had higher SMAD2/3 levels, with increased accumulation in the nucleus. CFIm25/ABCC1 codepleted cells, however, showed reduced SMAD2/3 expression and nuclear localization (Fig. 6D). These observations indicate that ABCC1 functions to enhance TGFB activity specifically in the context of CFIm25 loss. To further validate the requirement for TGFB signaling, we performed migration assays with CFIm25-depleted and CFIm25/ABCC1 codepleted cells and found that supplementing media with TGFB2 significantly rescues the migration of CFIM25/ABCC1 codepleted cells (Fig. 6E).

3′UTR shortening mediates posttranscriptional regulation of *ABCC1*

Having genetically and functionally established a role of ABCC1 for CFIm25-dependent cellular responses, we went on to assess the relevance of the short and long isoforms of ABCC1. Since quantification of total *ABCC1* mRNA showed no changes in overall levels (Fig. 7A), we assessed the localization and expression of ABCC1 protein by antibody staining in HCT116 KRAS G13D cells. As expected, we observed that ABCC1 localized to the plasma membrane by costaining the membrane protein GLUT1. In control cells, we also observed higher junctional localization of ABCC1, especially where they contacted each other, and a reduced expression pattern at cell "edges" that were not in contact with neighboring cells. In CFIm25-depleted cells, which display more spindle-like morphologies and lack cell-cell junctions, ABCC1 was evenly distributed along the plasma membrane (Fig. 7B and fig. S8A). ABCC1 KD caused a robust reduction in protein levels. Similar expression pattern changes were observed in DLD-1 KRAS G13D cells (fig. S8B), indicating that this redistribution of ABCC1 expression in CFIm25-depleted cells may hold important implications for cells undergoing EMT.

Given that there was no change in total *ABCC1* mRNA levels, we hypothesized that the specific 3′UTR isoforms might contribute to its posttranscriptional regulation. As a proxy for measuring protein output of the specific 3′UTR isoforms, the short and long 3′UTRs were cloned into a luciferase reporter construct (Fig. 7C). Luciferase activity was reduced by ~2-fold for the ABCC1 distal construct compared to the proximal construct, indicating that the long 3′UTR contains sequence elements that limit protein output, either through RNA degradation or reduced translation of the long isoform. qRT-PCR analysis of the luciferase transcript revealed that the long isoform showed decreased expression, confirming that this *ABCC1* isoform is less stable than the short one (Fig. 7D). Analysis of the distal 3′UTR of ABCC1 using TargetScan revealed overlapping consensus binding sites for microRNAs miR-145 (position 1728 to 1734) and miR-199a (position 1726 to 1733), which has been associated with regulating ABCC1 expression in breast cancers and sensitivity to chemotherapy (*49*). We deleted these microRNA binding sites in the distal 3′UTR construct but did not observe any changes in luciferase activity levels. These observations suggest that alternative mechanisms, either through other microRNAs or RBPs, serve to regulate the stability of the distal *ABCC1* isoform in this cell type. Given that CFIm25 depletion promotes an increase in proximal isoform expression accompanied by a comparable decrease in distal isoform, as observed in the RNA-seq data (Fig. 4G), we predict that this results in insignificant changes to overall transcript levels. However, the fraction of proximal isoform affords a more stable transcript as seen by luciferase activity and mRNA levels, which, in turn, has strong effects on EMT and cell migration (Fig. 8). Collectively, these results indicate that disrupting the balance of short and long *ABCC1* isoforms has profound consequences on the behavior of Ras-driven cells from nematode to human.

DISCUSSION

Understanding the cooperation between posttranscriptional regulatory mechanisms and activated oncogenes is an important challenge for identifying cancer dependencies that extend beyond genetic alterations. Here, we show that alternative polyadenylation functions as a highly conserved process in the modulation of oncogenic Ras output. Specifically, the APA factor *CFIM-1/CFIM25* functions to dampen hyperactive Ras-dependent output by biasing 3′UTR usage of multiple transcripts.

Loss of *cfim-1* results in 3′UTR shortening of numerous genes in *C. elegans* that increase the Muv phenotype with oncogenic gf mutations in the Ras ortholog *let-60*. Loss of *cfim-1* alone was insufficient to induce the Muv phenotype. Instead, *cfim-1* ablation enhanced Muv when the strong *let-60(n1046)* allele was suppressed by a reduction-of-function allele in the IGFR *daf-2* or in the weaker *let-60(ga89)* single mutant. Similarly, in isogenic colon cancer cells, CFIm25 depletion promoted the 3′UTR shortening of key oncogenes and induced EMT-like phenotypes both in Ras mutant and, to a lesser extent, in WT cells. However, increased migration and invasion were only observed in cells expressing mutant KRAS, suggesting that these alterations in the APA landscape cooperate with oncogenic Ras to modulate signaling output in both *C. elegans* and human cells. Studies have shown that thresholds of mutant KRAS activity dictate the progression of cancer and metastasis (*50*–*52*). We postulate that APA functions to lower the threshold for activated oncogene signaling in both organ development and cancer cell migration. However, how is oncogenic Ras output enhanced by biasing the APA landscape to shorter mRNA transcripts?

Although CFIm25 depletion has been associated with increased prevalence of cancer phenotypes in different tissues (*33*, *53*–*55*), our study provides mechanistic insights into how conserved genes such as the *mrp-5/ABCC* family of transporters that are subject to APA by CFIm25 cooperate with oncogenic Ras. Specifically, ablation of *mrp-5/ABCC1* suppressed the Muv phenotype in worms and migration of human cancer cells caused by *cfim-1*/*CFIm25* depletion, indicating that these are highly conserved determinants of oncogenic Ras

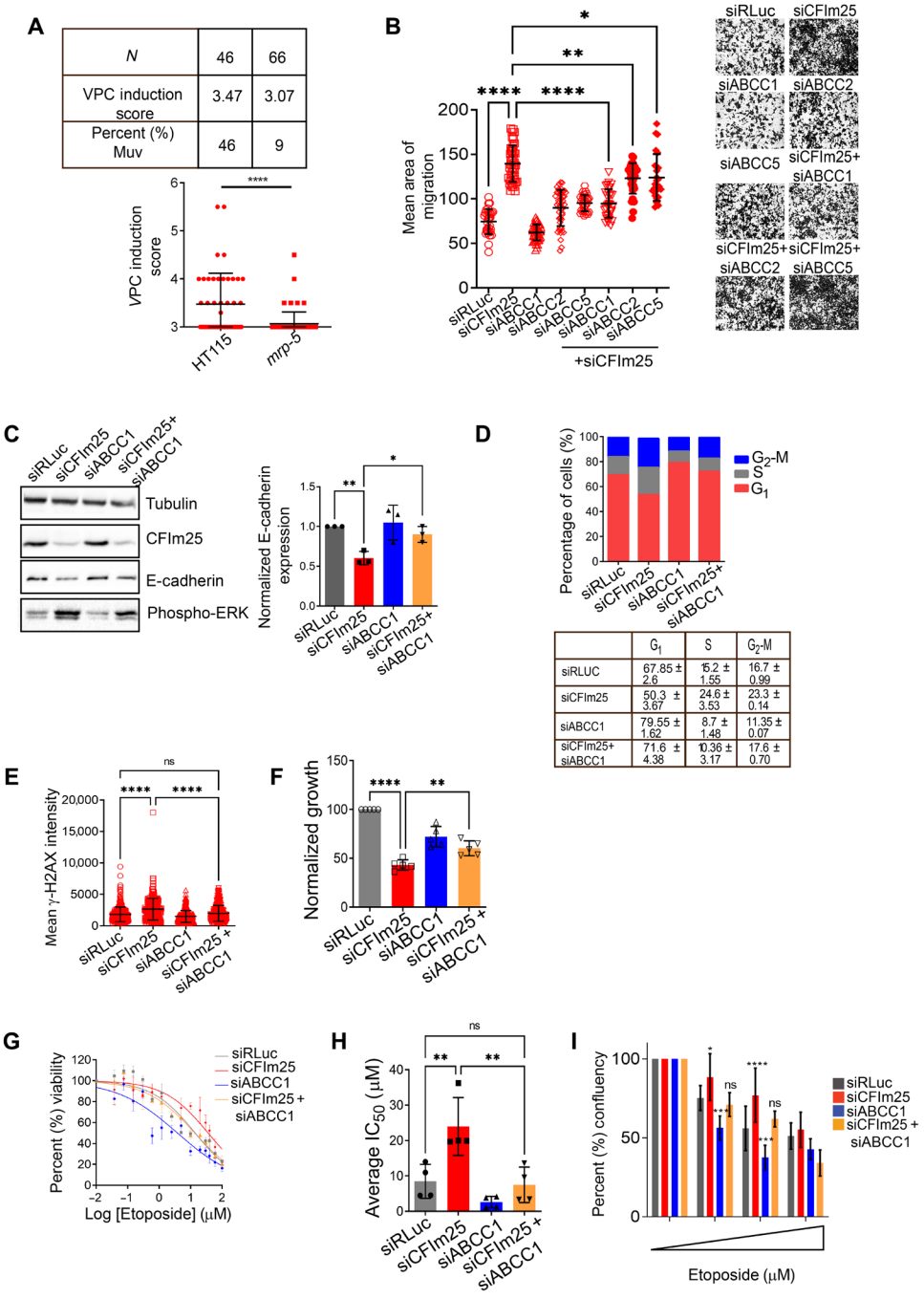

Fig. 5. Conserved transcripts regulate oncogenic Ras activity and tumorigenesis. (**A**) VPC induction scores of *let-60(gf); daf-2(lf); cfim-1(lf)* mutants on RNAi against *mrp-5*. Percent (%) Muv indicates the percentage of animals with more than three VPCs induced. *N* indicates the number of animals measured. *Y*-axis origin is set to 3 to represent the normal number of VPCs that are induced to divide. ****$P < 0.0001$, unpaired Student's *t* test. (**B**) Quantification of migration of KRAS G13D cells with either single depletion or codepletion of *CFIm25* and *ABBC1/2/5*. Each data point represents quantification of a field of view acquired across two independent experiments. Representative images are shown for each condition. Validation of KD is shown in fig. S7D. ****$P < 0.0001$, **$P < 0.01$, and *$P < 0.05$, one-way ANOVA with Tukey's post hoc test. (**C**) Representative Western blot of E-cadherin and phospho-ERK expression in KRAS G13D cell line transfected with the indicated siRNAs and quantification of E-cadherin protein levels normalized to tubulin across three independent experiments. (**D**) Cell cycle analysis of KRAS G13D transfected with the indicated siRNAs. Table depicts the proportion of cells in each phase ± SD across two independent experiments. (**E**) Quantification of γ-H2AX intensities in KRAS G13D cells transfected with indicated siRNAs. ****$P < 0.0001$, not significant, one-way ANOVA with Tukey's post hoc test. (**F**) Alamar Blue assay of KRAS G13D cells transfected with the indicated siRNAs. ****$P < 0.0001$ and **$P < 0.01$, one-way ANOVA with Tukey's post hoc test. (**G**) Representative IC_{50} calculation for KRAS G13D cells transfected with indicated siRNAs and treated with etoposide at increasing concentrations. Cell viability was measured using the Alamar Blue assay. (**H**) Average IC_{50} values for KRAS G13D cells calculated across four independent experiments. **$P < 0.01$, ns-nonsignificant, one-way ANOVA with Tukey's post hoc test. (**I**) Percent confluency of KRAS G13D transfected and treated with increasing concentrations of Etoposide-0, 3, 8 and 23μM (averages from Fig. 5H). ****$P < 0.0001$, ***$P < 0.001$, *$P < 0.05$, ns-nonsignificant, Two-way ANOVA with Tukey's post hoc test.

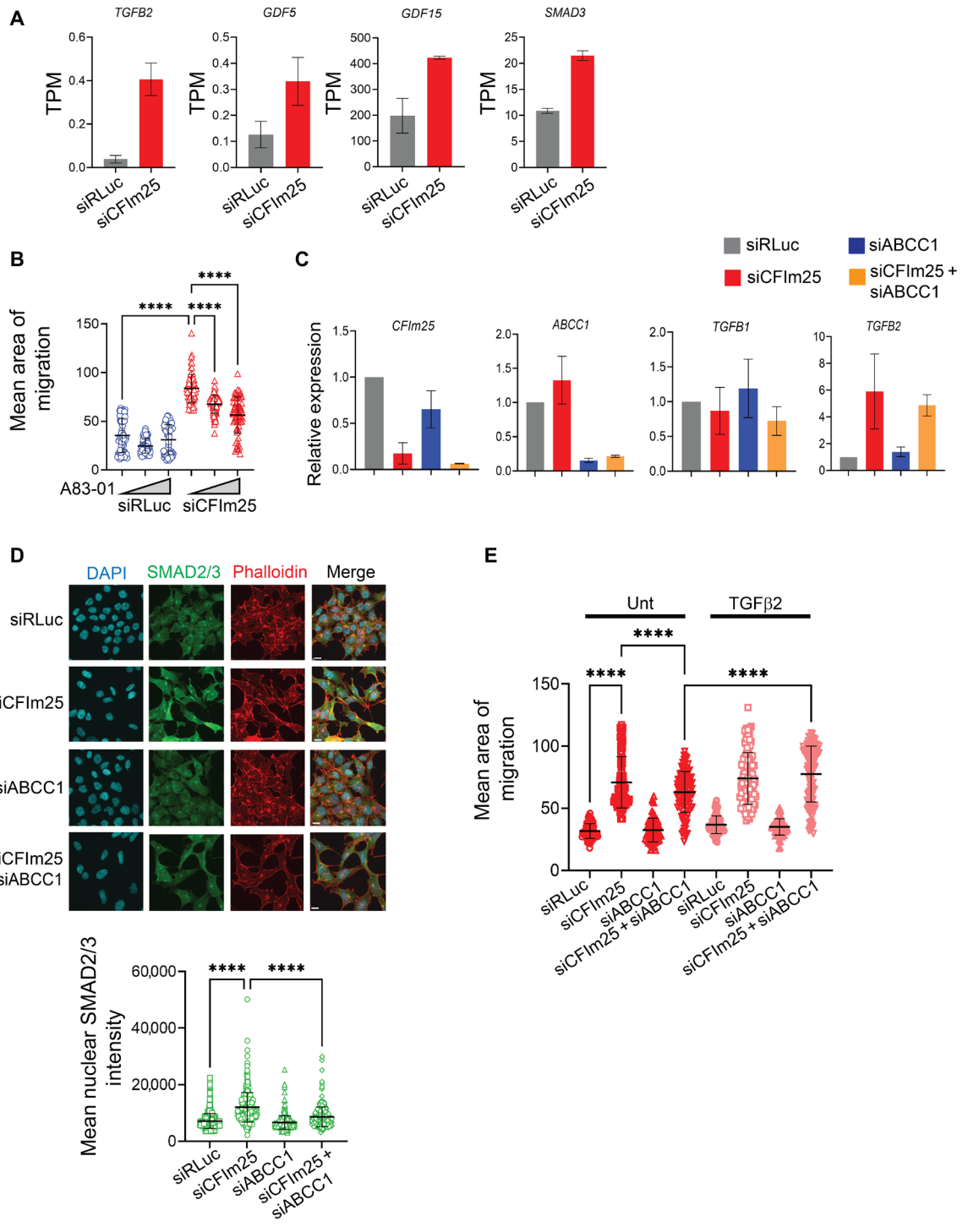

Fig. 6. ABCC1 cooperates with TGFB signaling to regulate cell migration. (**A**) Analysis of overall gene expression for *TGFB2*, *GDF5*, *GDF15*, and *SMAD3* in KRAS G13D RNA-seq data. $n = 3 \pm$ SD. (**B**) Quantification of migration of KRAS G13D cells transfected with indicated siRNAs and treated with A83-01 (0, 0.25, and 2.5 μM). Each data point represents a field of view captured across three independent experiments. ****$P < 0.0001$, not significant, two-way ANOVA with Tukey's post hoc test. (**C**) qRT-PCR analysis of CFIm25, ABCC1, TGFB1, and TGFB2 in cells transfected with the indicated siRNAS, $n = 2 \pm$ SD. (**D**) Representative confocal images and quantification of SMAD2/3 (green) in KRAS G13D cells transfected with the indicated siRNAS. Phalloidin (red) was used to stain actin, and DAPI (blue) was used to stain nuclei. Scale bars, 10 μm. Each data point represents a single nuclear quantification from two independent experiments. ****$P < 0.0001$, one-way ANOVA with Tukey's post hoc test. (**E**) Quantification of migration of KRAS G13D cells transfected with indicated siRNAs in the presence or absence of TGFB2 (10 ng/ml). Each data point represents a field of view captured across three independent experiments. ****$P < 0.0001$, two-way ANOVA with Tukey's post hoc test

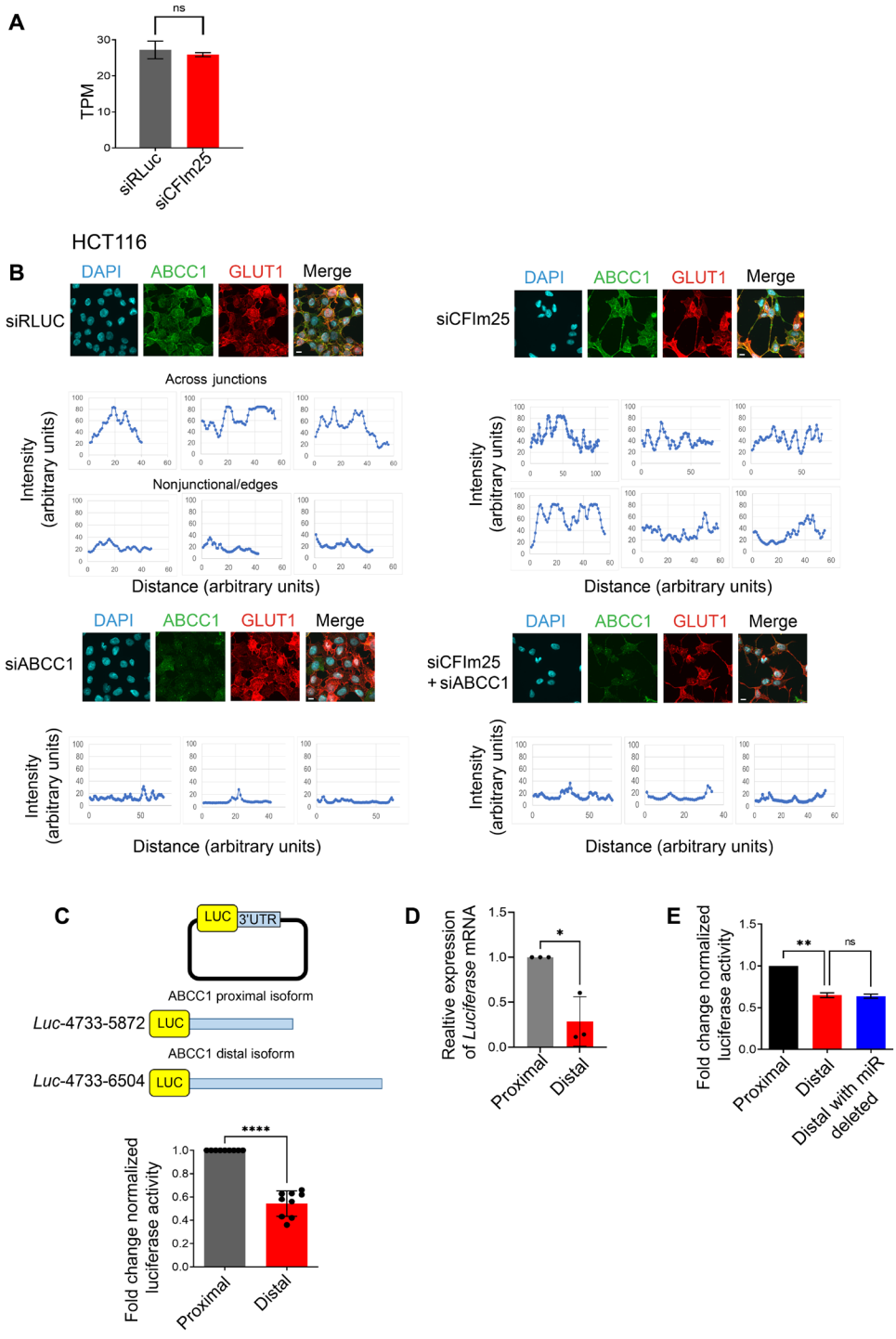

Fig. 7. 3′UTR sequence elements mediate posttranscriptional regulation of *ABCC1*. (**A**) Analysis of overall gene expression for *ABCC1* in KRAS G13D RNA-seq data. $n = 3 \pm$ SD. (**B**) Representative confocal images (maximum projection) of KRAS G13D cells transfected with the indicated siRNAs and stained for ABCC1 (green), GLUT1 (red), and DAPI (blue). Scale bars, 10 μm. Quantification of ABCC1 (intensity) was calculated by measuring the intensity profile across an ROI on cell membranes. In siRLuc samples, this included across cell junctions and cell edges. In siCFIm25 samples, random regions on cell membranes were selected. Additional images and quantifications for each condition are in fig. S8A. (**C**) Schematic representation of ABCC1 3′UTR luciferase reporter plasmids. Numbers denote the beginning and end of ABCC1 proximal or distal 3′UTR sequences. Quantification of Firefly luciferase activity for proximal and distal constructs normalized to Renilla luciferase (internal control). (**D**) qRT-PCR analysis for *Firefly Luciferase* expression performed for cells transfected with either proximal or distal *ABCC1* 3′UTR constructs normalized to *Renilla Luciferase* expression. *$P < 0.05$, unpaired Student's *t* test. (**E**) Quantification of Firefly luciferase activity for proximal, distal, and distal with miR site deletion. **$P < 0.01$, ****$P < 0.0001$, unpaired t-test; not significant.

output. The role of ABCC1 in cancers has been traditionally associated with multidrug resistance through the efflux of chemotherapeutic compounds such as etoposide and vincristine (*46*, *56*). High levels of ABCC1 transcript or protein have also been shown to correlate with drug resistance and increased metastasis of breast and other types of cancers (*57*), although the precise mechanisms of altered ABCC1 expression are unknown. Our study reveals that ABCC1 can regulate resistance to the topoisomerase inhibitor etoposide and cancer cell migration. Cancer cell migration, specifically, is dependent on TGFB signaling. Studies have shown that TGFB has a variety of roles in inducing EMT and drug resistance (*48*). Therefore, the identification of TGFB dependency in CFIm25-depleted cancer cells highlights a novel vulnerability that could be exploited for therapeutic purposes. Further studies are warranted to uncover the precise biochemical interaction between the ABCC1 membrane transporter and TGFB signaling.

The alterations in drug response and cell migration occur without overall changes in ABCC1 transcript. While we were unable to identify the precise microRNAs or RBPs that regulate transcript stability, it is apparent that the longer 3′UTR sequence contains elements that posttranscriptionally contribute to reduced expression of this isoform. Thus, the increase in proximal isoform expression and more uniform plasma membrane distribution of ABCC1 in CFIm25-depleted cells appear to hold important functional consequences for cells during EMT progression.

CFIm25 depletion affected the APA of hundreds of transcripts, suggesting that this posttranscriptional process serves to modulate expression thresholds of genes that function in multiple processes that orchestrate Ras-driven cellular behaviors. An example that we show in our study is the dependency on TGFB signaling. Therefore, identifying proteins/pathways affected by APA provides a unique opportunity to discover druggable targets to treat a variety of tumors. Given that these alterations would not be detectable using standard genome (DNA) sequencing technology, it highlights the importance of sequencing mRNA transcripts in patient samples.

Although ABCC1 is often amplified at the transcript or protein level in cancers, our study shows that ABCC1 is subject to a novel mode of regulation through alternative 3′UTR usage that does not alter transcript levels. We predict that this probably holds true for many novel genes that are not detected in standard gene expression studies. In support of this, a recent study using 3′-end sequencing of patient-derived chronic lymphocytic leukemia samples identified novel tumor suppressor genes altered through APA. These genes are not frequently mutated in cancer but have strong tumor suppressor functions, again highlighting the need to extend cancer-related studies beyond genomic DNA sequencing and standard gene expression analyses (*58*). This could be particularly important for pediatric cancers, where the mutational load is low compared with adult tumors (*59*). Model organisms such as *C. elegans* offer complementary and inexpensive in vivo systems to efficiently study the cooperation between activated oncogenes and APA factors. In addition, the array of genetic tools available in *C. elegans* offers many advantages for uncovering conserved genes that enforce oncogenic output relevant to human cancer. Our discovery of *mrp-5*/*ABCC1* serves as one such example and highlights the advantage of combining *C. elegans* with human cancer cells to accelerate the discovery of therapeutic targets to exploit cancer vulnerabilities.

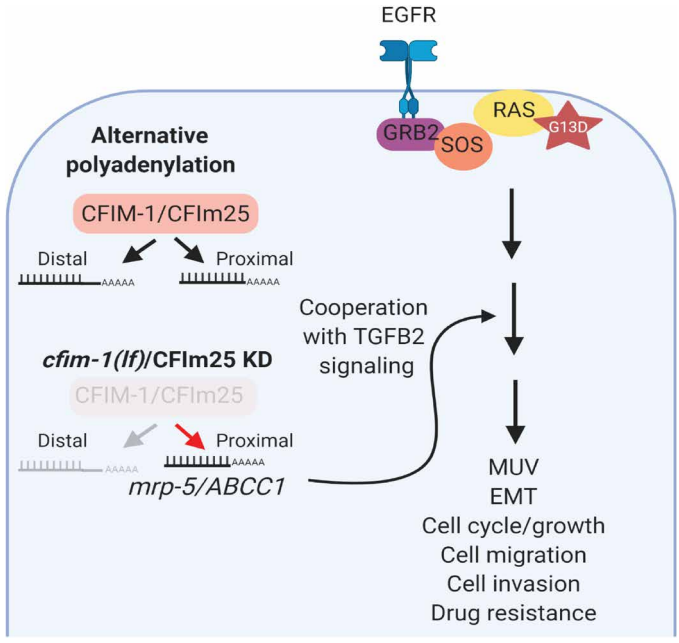

Fig. 8. Schematic model of CFIM-1/CFIm25 regulating oncogenic Ras signaling. CFIM-1/CFIm25 functions to regulate alternative polyadenylation of mRNA transcripts. Loss of CFIM-1/CFIm25 promotes 3′UTR shortening of genes such as *mrp-5* in *C. elegans* and its ortholog *ABCC1* in human cancer cells. ABCC1 cooperates with TGFB2 signaling to regulate oncogenic Ras signaling, thereby influencing EMT, cell migration, and drug response.

Table 3. List of *C. elegans* strains.

N2	WT
let-60(n1046)	Strong somatic Ras gain-of-function allele, (G13E substitution)
let-60(ga89)	Weaker gain-of-function Ras allele (L19F substitution)
daf-2(e1370)	*daf-2* loss of function
daf-16(mgDf47)	*daf-16* loss of function
cfim-1(on9)	*cfim-1(lf)* generated by CRISPR
daf-2(e1370); cfim-1(on9)	*daf-2(e1370)* crossed with *cfim-1(lf)*
let-60(n1046); daf-2(e1370)	*let-60(n1046)* crossed with *daf-2(e1370)*
let-60(n1046); daf-2(e1370); daf-16(mgDf47)	*let-60(n1046);daf-2(e1370)* crossed with *daf-16(mgDf47)*
let-60(n1046); daf-2(e1370); cfim-1(on9)	*let-60(n1046); daf-2*(e1370) crossed with *cfim-1(lf)*
let-60(ga89); cfim-1(on9)	*let-60(ga89)* crossed with *cfim-1(lf)*

MATERIALS AND METHODS

Crosses to generate double and triple mutants

All crosses were performed by plating 3 to 5 hermaphrodites with 10 to 15 males on petri dishes filled with nematode growth media (NGM) containing a bacterial lawn. Approximately five F1 hermaphrodites at the L4 stage of development were then plated onto NGM plates. F2 progeny were collected at the L4 stage of development and

singled out onto separate NGM plates. F2 worms were incubated until they laid eggs to propagate the strain, and then the F2 parents were collected and lysed. The worm lysate was used for PCR reactions to confirm the presence of the desired genetic lesion.

Quantification of the multivulva phenotype

The multivulva phenotype was scored on the basis of the degree of vulva induction. Vulva induction refers to the number of VPCs induced to form part of the vulva at the L2 stage of development. This is measured by visualizing the VPC daughter cells at the L4 stage of development. Visualization was performed using a Leica DMRA2 compound light microscope with differential interference contrast (DIC) optics at ×63 magnification. Worms were mounted on glass slides with 4% agarose pads and anesthetized using 20 mM tetramisole. Primary VPCs undergo three rounds of cell division and comprise eight daughter cells, secondary daughter cells undergo eight rounds of division and comprise seven daughter cells, and tertiary VPCs undergo one round of division and comprise two daughter cells. These daughter cells and the pattern they form are easily visualized by DIC microscopy at ×63 magnification. A normal vulva develops from one primary and two secondary vulva cells, which are assigned an induction score of 3.0 since three VPCs have been induced. Worms with a Muv phenotype often have tertiary VPCs induced to partial primary and secondary fates, which have only three to four vulva cell daughters developing into pseudovulvae. These are given an induction score of 0.5 as "half" of a vulval cell has been induced in these cases. In addition to induction scores, the percentage of Muv worms of various genotypes was calculated. In cases where induction scores were calculated, % Muv was calculated by dividing the number of worms with induction scores more than 3.0 by the total number of worms measured. In cases where no induction scores were calculated, % Muv was calculated by quantifying all worms with at least one pseudovulva and dividing this number by the total number of adult worms. All worms scored for vulva induction were raised at 20°C, with the exception of the *let-60(gf); daf-2(lf); cfim-1(lf)* strain, which was raised at 16°C.

RNAi feeding protocol

RNAi cultures were obtained from the Source Bioscience *C. elegans* RNAi library. Bacteria were struck onto LB plates containing ampicillin and tetracycline (working concentrations of 50 and 5 mg/ml, respectively). Plates were incubated overnight at 37°C. Single colonies were picked and inoculated in liquid $LB^{amp+tet}$ overnight at 37°C with shaking. Following the overnight inoculation, isopropyl β-D-1-thiogalactopyranoside (IPTG) was added to each culture (0.5 μM) and incubated at 37°C with shaking for 4 hours. The bacterial culture was then concentrated 2× or 10× by centrifugation and mixing. The culture was then plated on solid NGM media with added carbenicillin and IPTG (working concentrations of 25 μg/ml and 25 mM, respectively). Worms were added to these RNAi plates at the L4 stage, and measurements were taken of the F1 progeny.

Candidate RNAi screening protocol

For the screening of DAF-16 target genes, single colonies of each RNAi from the Source Bioscience *C. elegans* RNAi library were inoculated into liquid LB media and induced with IPTG as described in the "RNAi feeding protocol" section. Bacterial cultures were plated onto 12-well plastic plates filled with solid NGM RNAi media so that each well contained a different RNAi bacteria strain. Each plate also included one well with negative control bacteria (HT115) and a positive control bacterial strain expressing *daf-16* RNAi. Bacterial lawns were grown overnight at 37°C, and two L4 stage *daf-2(e1370); let-60(n1046)* double mutant worms were picked into each well. Worms were grown until pseudovulvae could be seen with a dissecting microscope in the *daf-16* RNAi–positive control well. Plates were then scanned through the rest of the wells, noting RNAi treatments that resulted in worms being noticeably more Muv than the negative controls and appearing similar to worms treated with *daf-16* RNAi. Each plate was replicated, and a positive hit was only scored if a Muv phenotype could be seen in both replicates. Positive hits were subjected to a more stringent analysis by calculating vulval induction scores described in the "Quantification of the multivulva phenotype" section. The candidate RNAi strains were grown and concentrated 2× and then plated onto 10-cm solid NGM RNAi media plates. We plated three to four *daf-2(e1370); let-60(n1046)* L4 worms onto these plates and quantitated vulva induction scored for 15 to 20 F1 progeny under ×63 magnification.

For the screen of genes with shortened 3′UTRs, RNAi cultures were grown overnight and induced with IPTG for 4 hours. Cultures were then concentrated 10× and plated onto NGM plates. Four to five *let-60(n1046); daf-2(e1370); cfim-1(on9)* L4 worms were picked onto each RNAi plate, and % Muv was calculated in the F1 generation. Only those RNAi treatments that were able to produce a significant increase in Muv induction compared to the negative controls HT115 were considered positive hits.

Generation of CRISPR strains

The *cfim-1(lf)* CRIPSR strain was created with CRISPR technology using the self-excising drug selection cassette as previously described (*60*). The "aaacctccg" sequence at position 79 from the *cfim-1* start codon was mutated by deleting the 5–base pair (bp) "aaacc" and changing "tccg" to "tagt" to create frameshift and a premature stop codon (TAG).

RNA extraction

For *C. elegans* samples, RNA was extracted from L4 stage worms using TRIzol (Invitrogen). RNA from human cancer cells was extracted 48 hours after transfection using the RNeasy Kit from QIAGEN according to the manufacturer's instructions.

RNA-seq library preparation and sequencing

To construct RNA-seq libraries from *C. elegans* samples, we used an automated QuantSeq 3′mRNA-seq (Lexogen GmbH, Vienna) using the Agilent NGS Workstation (Agilent Technologies, Santa Clara) as per the manufacturer's protocol. Briefly, 250 ng of total RNA was used to generate complementary DNA (cDNA). cDNA was amplified with 17 PCR cycles as determined by qPCR analysis using the PCR Add-on Kit (Lexogen). External RNA Controls Consortium (ERCC) RNA spike-ins were added following the manufacturer's instructions. The resulting libraries were quantified with Qubit DNA HS (Thermo Fisher Scientific, Waltham), and fragment sizes were analyzed on the Agilent Bioanalyzer using the High-Sensitivity DNA assay before sequencing. Sequencing was performed at The Centre for Applied Genomics (Hospital for Sick Children, Toronto) across two lanes of an Illumina HiSeq2500 rapid run flowcell (Illumina, San Diego) with SR100 bp.

For sequencing of human cancer cell samples, total RNA was treated with the DNA-free DNA Removal Kit (catalog no. AM1906,

Thermo Fisher Scientific Inc., Waltham, USA) to remove contaminant DNA. Deoxyribonuclease-treated total RNA was then quantified using Qubit RNA BR (catalog no. Q10211, Thermo Fisher Scientific Inc., Waltham, USA) fluorescent chemistry, and 1 ng was used to obtain RNA integrity number (RIN) using the Bioanalyzer RNA 6000 Pico Kit (catalog no. 5067-1513, Agilent Technologies Inc., Santa Clara, USA). The lowest RIN was 9.1; median RIN score was 9.8. A total of 1000 ng per sample was then processed using the TruSeq Stranded mRNA Library Prep (catalog no. 20020595, Illumina Inc., San Diego, USA; protocol v. 1000000040498 v00) including poly(A) selection, with 8 min of fragmentation at 94°C and 15 cycles of amplification. Top stock (1 μl) of each purified final library was run on an Agilent Bioanalyzer Double-stranded DNA (dsDNA) High-Sensitivity chip (catalog no. 5067-4626, Agilent Technologies Inc., Santa Clara, USA). The libraries were quantified using the NEBNext Library Quant Kit for Illumina (catalog no. E7630L, New England Biolabs, Ipswich, USA) and were pooled at equimolar ratios after size adjustment. The final pool was run on an Agilent Bioanalyzer dsDNA High-Sensitivity chip and quantified using the NEBNext Library Quant Kit. The quantified pool was hybridized at a final concentration of 2.2 pM and sequenced on the Illumina NextSeq 500 platform using two High-Output v2 flowcells for an average of 85 million 1 × 85 bp reads.

Analysis of 3′UTRs

C. elegans

Sequencing read processing. Single-end sequencing reads of 144 bp were obtained. Reads were trimmed using Cutadapt as follows: (i) First, 12 bp of reads were trimmed, (ii) base pairs with a sequencing quality lower than 30 were trimmed from the ends of reads, and (iii) poly(A) stretches at the end of reads were trimmed using 10 A's as an "adaptor" sequence. Only reads with at least 5 A's trimmed at the ends are used for subsequent analysis. ERCC transcripts were only used to ensure library quality and were not included in the subsequent analyses.

PA site identification. The 3′ most nucleotide of each read was used to create a track of reads pile-up. R package "derfinder" (version 1.12.0) (*61*) was used to identify expressed regions separately for reads that mapped to the positive or the negative strand. Essentially, any consecutive positions with more than 1 RPM (reads per million mapped reads) were identified as an expressed region. Regions were extended 5 bp upstream. Regions that are within 5 bp from each other were then merged.

Poly(A) clusters were then mapped to *C. elegans* gene annotation (WBcel235, obtained from Ensembl 85). Meanwhile, sequence composition downstream of each ER was examined to identify expressed regions that potentially originated from internal poly(A) priming events. Specifically, two criteria are used: (i) within 30 bp downstream and 5 bp upstream from each expressed region end, if the pattern of 18 As (allowing five mismatches) can be found; (ii) within 10 bp downstream and 5 bp upstream from each expressed region end, if the frequency of As is larger or equals to 60%. In addition, 35 bp upstream from each expressed region end, we searched for the two most common poly(A) signals, AATAAA and ATTAAA.

PA site annotation. Expressed regions that map to exons are annotated to the associated genes. Expressed regions that do not map to exons are annotated with the following steps:

1) Expressed regions that are within 3 kb from the nearest transcript end site (TES) upstream are annotated to the corresponding gene.

2) Expressed regions that map to introns are annotated to the associated genes.

3) In the rare case that an expressed region maps both to an intron and downstream of a gene, if the expressed regions maps within 200 bp of a gene's TES, then it is annotated to that gene; otherwise, it is annotated to the intron-containing gene.

Last, all annotations are merged, and the number of reads mapped to each expressed region is then calculated.

Identify alternative PA sites per gene. We systematically processed PA sites that mapped to each gene and used stringent criteria to analyze only confident PA sites. We consider a few different situations:

1) PA sites that are likely derived from internal poly(A)s are discarded even if the PA site is mapped to exons.

2) An exception to (i): If an internal poly(A)–derived site (determined in the "PA site annotation" section) is the longest potential PA site or the second longest PA site followed by a real PA site and also contains a significant proportion (more than 50%) of all reads mapped to this gene, then it is considered a "valid PA site." In these two cases, although we cannot precisely pinpoint PA sites [because of internal poly(A) priming within the 3′UTR], we have high confidence that this poly(A) signal is derived from the longest 3′UTR variant (because no signal is detected downstream) and can be used to assay alternative PAs (APAs).

3) If more than 75% of the reads mapped to this gene map to internal poly(A)–derived sites, then this gene is not considered for APA analysis.

4) If potential PA sites are within 15 bp of each other, then merge them.

5) After merging, only keep the PA sites containing more than 5% of all the mapped reads of this gene and have more than 10 reads in at least three samples for further analysis. The purpose is to filter out extremely weak PA signals.

6) Last, genes with more than one PA site after the filtering are subjected to DEXSeq analysis.

We order and name the PA sites based on their relative positions along the gene body, and "E001" refers to the most proximal PA site. Proximal polyadenylation site usage (PPAU) is calculated as the number of reads mapping to the most proximal PA site/total number of reads mapping to all valid PA sites of the gene.

APA analysis. To characterize genes that undergo APA, we used the R package "DEXSeq" (version 1.24.2) (*62*) and examined every pair of comparisons. We applied a cutoff of adjusted P value of <0.05. To summarize the results, we only considered the comparisons between N2 (the WT) and *cfim-1* mutants. For each gene in each comparison, we annotate on the basis of its APA condition. The top four primary situations are as follows: (i) The most proximal PA site is expressed higher in WT; (ii) at least one of the more distal PA sites is expressed higher in mutants; (iii) the most proximal PA site is expressed higher in WT, and at least one more distal PA site is expressed higher in mutants; and (iv) the most proximal PA site is expressed higher in mutants, and at least one more distal PA site is expressed higher in the WT. Other more complicated APA cases were not specifically classified and are represented as "others."

Gene expression analysis. First, the number of reads mapped to each gene was counted by adding the reads in expressed regions that mapped to (i) any exons and (ii) being annotated to this gene and passed the internal poly(A) filtering criteria (described in the "PA site identification" section). Next, normalized read count was obtained using the fpm() function from R package "DESeq2" (version 1.24.0) (*63*).

Data for PPAU and classification of APA events identified can be found in files S9 and S10.

Homo sapiens

Quantification of 3′UTR isoforms. To estimate 3′UTR isoform abundances, we used the alternative polyadenylation analysis tool QAPA version 1.2.0 (*41*). In short, QAPA constructs a refined set of 3′UTR isoforms from the GENCODE basic gene annotations using external databases of polyadenylation sites (*64*). Next, QAPA selects 3′UTRs from the most downstream exon of the gene to resolve ambiguities in quantification of 3′UTR isoforms with reads generated by RNA-seq. Using this refined 3′UTR annotation library, we quantified 3′UTR isoforms using raw RNA-seq reads with the alignment-free isoform quantification tool Sailfish version 0.10.0 (*65*). On the basis of mRNA quantification from biological replicates per each cell type, we calculated the average, SD, and coefficient of variation for each 3′UTR isoform.

APA analysis. Abundance of 3′UTR isoforms was quantified in transcripts per million (TPM column in Sailfish output). To classify genes into APA patterns, we considered $\log_2$ fold change (FC) and *Z* scores between CFIm25 (NUDT21) KD and control conditions for both WT and mutant KRAS samples using the following equation

$$Z = \sqrt{n}\,|\,\mathrm{TPM}^{\mathrm{KD}}_{\mathrm{mean}} - \mathrm{TPM}^{\mathrm{CTRL}}_{\mathrm{mean}}\,|\,/\,\sqrt{\mathrm{TPM}^{\mathrm{KD}}_{\mathrm{var}} + \mathrm{TPM}^{\mathrm{CTRL}}_{\mathrm{var}}}$$
$$\log_2\mathrm{FC} = \log_2\frac{\mathrm{TPM}^{\mathrm{KD}}_{\mathrm{mean}}}{\mathrm{TPM}^{\mathrm{CTRL}}_{\mathrm{mean}}} \quad (1)$$

where *n* is number of samples (3 in this experiment) and $\mathrm{TPM}_{\mathrm{mean}}$ and $\mathrm{TPM}_{\mathrm{var}}$ are the TPM average and SD based on replicates. Shift patterns were categorized into three groups based on *Z* and $\log_2\mathrm{FC}_{\mathrm{TPM}}$: switches, proximals, and distals.

Switches are defined as genes with a reciprocal shift in any pair of the 3′UTR isoforms. One isoform changes by $\log_2\mathrm{FC}_{\mathrm{TPM}} > \log_2(1.5)$ and $Z > 2$, and another isoform changes by $\log_2\mathrm{FC}_{\mathrm{TPM}} < -\log_2(1.5)$ and $Z > 2$.

Proximals are defined as genes with a shift only in the shortest 3′UTR, corresponding to proximal pA site. Only the shortest 3′UTR changes by $\mathrm{abs}(\log_2\mathrm{FC}_{\mathrm{TPM}}) > \log_2(1.5)$ and $Z > 2$.

Distals are defined as genes with a shift in only one 3′UTR isoform, corresponding to any distal pA site. Only one distal 3′UTR changes by $\mathrm{abs}(\log_2\mathrm{FC}_{\mathrm{TPM}}) > \log_2(1.5)$ and $Z > 2$.

Last, we select genes with an increase in proximal 3′UTR among the genes captured in the way described above. Proximal 3′UTR changes by $\log_2\mathrm{FC}_{\mathrm{TPM}} > \log_2(1.5)$ and $Z > 2$. A shift of $\log_2(1.5)$ means that abundance is higher in CFIm25 KD than in control. These genes were used for comparisons with *C. elegans* 3′UTR results. QAPA data, classification of APA events detected, PPAU, and gene expression data can be found in files S11 to S14.

Gene ontology analysis

C. elegans genes were classified into biological categories by selecting the gene ontology biological function on Genemania. For overlapping with human dataset, *C. elegans* genes were converted into their human orthologs in Ortholist 2.0 (*43*). The resulting orthologs were used for subsequent IPA analysis or overlaid with human dataset to identify commonly regulated genes. IPA was performed on both human and worm-converted genes to classify genes into signaling pathways. Ortholist analysis can be found in file S15.

Cell culture

HCT116 KRAS G13D, KRAS WT cells, and DLD-1 cells were maintained in McCoy's 5A medium supplemented with 10% fetal bovine serum (FBS). Pancreatic BXPC3, CFPAC-I, and HPAF-II cell lines were grown in Dulbecco's modified Eagle's medium supplemented with 10% FBS. Cell lines were validated by STR profiling.

siRNA transfection

For siRNA KD experiments, 300,000 cells per well were plated on six-well plates and transfected with pooled siRNA at a final concentration of 25 nM using Lipofectamine RNAiMAX according to the manufacturer's instructions. All siRNAs were obtained from Dharmacon.

Growth assay

For growth assays, cells were harvested 24 hours after transfection and counted, and 3000 cells per well were plated on 96-well plates. Growth was measured using Presto Blue (Invitrogen), and fluorescence was measured using a plate reader according to the manufacturer's instructions. Readings were taken at 0, 24, 48, and 72 hours after plating for time course experiments.

Cell cycle analysis

Cell cycle analysis was performed using the Click-iT Plus EdU Alexa Fluor 647 Flow Cytometry Assay Kit (Thermo Fisher Scientific). To obtain the cell cycle profile, HCT116 cells with and without CFIm25 KD (72 hours) were pulse labeled with 10 μM EdU for 2 hours. The cells were then harvested and fixed by adding ice-cold ethanol dropwise to the cells. The cells were then permeabilized and washed, and Click-iT EdU was detected using the manufacturer's protocol. Cells were lastly suspended in 0.5 ml of FxCycle propidium iodide/ribonuclease staining solution (Invitrogen). Samples were analyzed on a Fortessa flow cytometer.

Cell migration and invasion assays

Cells were harvested 24 hours after transfections and counted, and 80,000 cells were plated on top of a transwell 8 μM insert in low (0.1% FBS) media. Complete media (10% FBS) was placed in the well below the insert. Each condition was performed in triplicate. Cells were allowed to migrate for 20 hours before fixing and staining with 1% Crystal Violet in 20% methanol for 20 min at room temperature. For migration assays related to TGFB signaling, transfected cells were pretreated with A83-01 overnight at indicated concentrations before being plated for migration assays in low FBS media supplemented with the indicated concentrations of A83-01 (Selleckchem). Double-transfected cells were plated for migration in low FBS media with or without TGFB2 (10 ng/ml; Cell Signaling Technologies). The top layer of the transwell membrane was scraped to remove excess stain and washed with phosphate-buffered saline (PBS). Inserts were allowed to dry before imaging on a Nikon epifluorescence microscope using a 10× objective. At least five fields of view were acquired per insert, and the area of migrated cells was calculated using ImageJ and represented as the mean area of migration. For invasion assays, Matrigel (150 $\mu g/cm^2$) was added to the top of each insert and allowed to solidify before plating cells. Fixation and imaging were performed as described above.

Drug assays

Cells were transfected on 6-well plates, and a total of 5000 cells per well were plated onto 96-well plates after 24 hours. Cells were allowed to adhere overnight and then treated with increasing doses of etoposide (Tocris Bioscience) and Camptothecin (Selleckchem) for a further 48 hours. Cell viability was measured using Alamar Blue assay. Median inhibitory concentration (IC_{50}) curves were generated, and calculations were performed using GraphPad Prism 6.0 software.

To calculate the confluency of cells after drug treatment, cells were transfected on six-well plates and treated with etoposide at increasing doses for 48 hours. Cells were then stained with 1% Crystal Violet in 20% methanol and air-dried. Five random fields of view were acquired for each condition, and the area covered by cells was quantified using ImageJ.

Immunofluorescence

Cells were transfected for 24 hours and then harvested, and 100,000 cells were plated on poly-L-lysine–coated glass coverslips for a further 48 hours. Cells were fixed in 4% paraformaldehyde, permeabilized with 0.1% Triton X/PBS for 5 min, and blocked for 1 hour with 10% goat serum/1% bovine serum albumin solution. Coverslips were then incubated overnight at 4°C with the primary antibody anti-Vimentin (1:1000; BioLegend). Coverslips were washed and stained with the secondary antibody goat anti-chicken Alexa Fluor 488 for 1 hour at room temperature. Cells were stained with 4′,6-diamidino-2-phenylindole (DAPI; 1:1000) for 5 min. Coverslips were washed and mounted using ProLong Gold Antifade Mountant. Cells were imaged on a Quorum spinning disk confocal microscope using the 40× objective.

For γ-H2AX staining, cells were fixed and stained with anti–γ-H2AX antibody (1:500; Sigma-Aldrich), followed by staining with a goat anti-mouse Alexa Fluor 568 and DAPI, and imaged on a Quorum spinning disk confocal microscope using the 40× objective. Quantification of mean γ-H2AX signal was performed using the Volocity analysis software. Total nuclear area was identified using DAPI staining, and mean red intensities were calculated. Regions of interests (ROIs) were randomly selected to quantify background signal, which was subtracted from the total intensity values.

For SMAD2/3 staining, cells were fixed and stained with anti-SMAD2/3 antibody (1:200; Cell Signaling Technologies), followed by staining with a goat anti-rabbit Alexa Fluor 488, phalloidin-568 (1:1000; Invitrogen), and DAPI. Cells were imaged on a Quorum spinning disk confocal microscope using the 40× objective. Quantification of mean SMAD2/3 in nuclei was performed using the Volocity analysis software. Total nuclear area was identified using DAPI staining, and mean green intensities were calculated. ROIs were randomly selected to quantify background signal, which was subtracted from the total intensity values.

For assessing ABCC1 expression, cells were fixed in a 1:1 ratio of methanol and acetone. Cells were then stained with anti-ABCC1 antibody (1:50; Monosan) for 1 hour at room temperature followed by staining with a donkey anti-rat Alexa Fluor 488 antibody. Cells were also costained with anti-Glut1 antibody (1:200; Abcam) followed by a goat anti-rabbit Alexa Fluor 568. Cells were imaged on a Quorum spinning disk confocal microscope using the 40× objective. For quantification, ROIs were randomly selected along cell membranes. The "plot profile" function on ImageJ was used to calculate the intensity of signal along ROIs.

Western blotting

Cells were lysed in 1% NP-40 lysis buffer containing 5 M NaCl, 10% NP-40, and 1 M tris (pH 8.0) supplemented with protease and phosphatase inhibitors. Lysates were cleared by centrifuging at maximum speed. Protein concentration was determined by using the BCA assay (Thermo Fisher Scientific). Protein (30 μg) was loaded and run on 10% Mini-PROTEAN TGX Precast Protein Gels (Bio-Rad). Separated proteins were transferred onto nitrocellulose membranes (Bio-Rad) and blocked with 5% bovine serum albumin for 1 hour, followed by incubation with primary antibodies overnight at 4°C. Following three washes with 0.1% Tween 20 in tris-buffered saline, membranes were incubated with horseradish peroxidase–conjugated secondary antibodies for 1 hour at room temperature. Blots were washed and developed using enhanced chemiluminescence substrate (Thermo Fisher Scientific). The following antibodies were used: anti-NUDT21 (1:1000; Proteintech), anti-tubulin (1:5000; Sigma-Aldrich), anti–E-cadherin (1:1000; Cell Signaling Technology), and anti–phospho-ERK (1:1000; Cell Signaling Technology).

Quantitative reverse transcription polymerase chain reaction

cDNA was reverse-transcribed using the SuperScript III Reverse Transcriptase Kit (Thermo Fisher Scientific), and qPCR was performed using the ssoAdvanced Universal SYBR Green Supermix (Bio-Rad). Primer sequences are included in Table 4.

Table 4. List of qRT-PCR primers.

	Forward (5′-3′)	Reverse (5′-3′)
18S	GATTAAGTCCCTGCCCTTTGTACA	GATCCGAGGGCCTCACTAAAC
CFIm25	TGCAGCTGGGAACAACTT	TGACGACCCAGTATCTCTGT
ABCC1	TGGACCTGTTTCGTGACATC	AGGGATTAGGGTCGTGGAT
ABCC2	CAGCTGGTATGACAGCATCA	GCTTTCTGCAGCTCTCTCTT
ABCC5	CGAAGGGTTGTGTGGATCTT	TTTCACCATGAAGGCTGGTC
Firefly Luciferase	GCAGAAGAAGCTGCCTATCA	GGCAGATGAGATGTCACGAA
Renilla Luciferase	AAAGCGAAGAGGGCGA GAA	TGCGGACAATCTGGAC GAC
TGFB1	GATGTCACCGGAGTTGTGCG	AGTGAACCCGTTGATGTCCACT
TGFB2	GCCTGAACAACGGATTGAGC	ATCGAAGGAGAGCCATTCGC

Luciferase assays

The long and short 3′UTRs cloned into the dual-luciferase vector miTarget vector were obtained from GeneCopoeia. HCT116 cells were plated on six-well plates and transfected with 50 ng of each plasmid. Luciferase expression was measured after 48 hours using the Dual Luciferase Assay System (Promega). Transfected cells were also collected for RNA extraction and qRT-PCR analysis as described above.

Site-directed mutagenesis

Site-directed mutagenesis of the long ABCC1 3′UTR construct was performed using the QuikChange II XL Site-Directed Mutagenesis Kit from Agilent according to the manufacturer's protocol.

Statistical analysis

All statistical analysis was performed as indicated on GraphPad Prism.

Creation of schematic representations

All schematic representations were created with BioRender.com.

SUPPLEMENTARY MATERIALS

Supplementary material for this article is available at https://science.org/doi/10.1126/sciadv.abh0562

View/request a protocol for this paper from *Bio-protocol*.

REFERENCES AND NOTES

1. A. Sud, B. Kinnersley, R. S. Houlston, Genome-wide association studies of cancer: Current insights and future perspectives. *Nat. Rev. Cancer* **17**, 692–704 (2017).
2. Y. Pylayeva-Gupta, E. Grabocka, D. Bar-Sagi, RAS oncogenes: Weaving a tumorigenic web. *Nat. Rev. Cancer* **11**, 761–774 (2011).
3. K. Haigis, K. R. Kendall, Y. Wang, A. Cheung, M. C. Haigis, J. N. Glickman, M. Niwa-Kawakita, A. Sweet-Cordero, J. Sebolt-Leopold, K. M. Shannon, J. Settleman, M. Giovannini, T. Jacks, Differential effects of oncogenic K-Ras and N-Ras on proliferation, differentiation and tumor progression in the colon. *Nat. Genet.* **40**, 600–608 (2008).
4. G. A. Hobbs, C. J. Der, K. L. Rossman, RAS isoforms and mutations in cancer at a glance. *J. Cell Sci.* **129**, 1287–1292 (2016).
5. D. Tuveson, A. T. Shaw, N. A. Willis, D. P. Silver, E. L. Jackson, S. Chang, K. L. Mercer, R. Grochow, H. Hock, D. Crowley, S. R. Hingorani, T. Zaks, C. King, M. A. Jacobetz, L. Wang, R. T. Bronson, S. H. Orkin, R. A. De Pinho, T. Jacks, Endogenous oncogenic K-ras(G12D) stimulates proliferation and widespread neoplastic and developmental defects. *Cancer Cell* **5**, 375–387 (2004).
6. R. Fragoso, T. Mao, S. Wang, S. Schaffert, X. Gong, S. Yue, R. Luong, H. Min, Y. Yashiro-Ohtani, M. Davis, W. Pear, C. Z. Chen, Modulating the strength and threshold of NOTCH oncogenic signals by mir-181a-1/b-1. *PLOS Genet.* **8**, e1002855 (2012).
7. D. J. Murphy, M. R. Junttila, L. Pouyet, A. Karnezis, K. Shchors, D. A. Bui, L. Brown-Swigart, L. Johnson, G. I. Evan, Distinct thresholds govern Myc's biological output in vivo. *Cancer Cell* **14**, 447–457 (2008).
8. M. Giam, G. Rancati, Aneuploidy and chromosomal instability in cancer: A jackpot to chaos. *Cell Div.* **10**, 3 (2015).
9. M. Han, R. V. Aorian, P. W. Sternberg, The let-60 locus controls the switch between vulval and nonvulval cell fates in Caenorhabditis elegans. *Genetics* **126**, 899–913 (1990).
10. P. W. Sternberg, M. Han, Genetics of RAS signaling in *C. elegans*. *Trends Genet.* **14**, 466–472 (1998).
11. M. B. Ryan, R. B. Corcoran, Therapeutic strategies to target RAS-mutant cancers. *Nat. Rev. Clin. Oncol.* **15**, 709–720 (2018).
12. J. M. Kirkwood, L. Bastholt, C. Robert, J. Sosman, J. Larkin, P. Hersey, M. Middleton, M. Cantarini, V. Zazulina, K. Kemsley, R. Dummer, Phase II, open-label, randomized trial of the MEK1/2 inhibitor selumetinib as monotherapy versus temozolomide in patients with advanced melanoma. *Clin. Cancer Res.* **18**, 555–567 (2012).
13. A. D. Cox, S. W. Fesik, A. C. Kimmelman, J. Luo, C. J. Der, Drugging the undruggable Ras: Mission possible? *Nat. Rev. Drug Discov.* **13**, 828–851 (2014).
14. D. C. Di Giammartino, K. Nishida, J. L. Manley, Mechanisms and consequences of alternative polyadenylation. *Mol. Cell* **43**, 853–866 (2011).
15. C. Mayr, What are 3′ utrs doing? *Cold Spring Harb Perspect. Biol.* **11**, a034728 (2019).
16. R. Sandberg, J. R. Neilson, A. Sarma, P. A. Sharp, C. B. Burge, Proliferating cells express mRNAs with shortened 3′ untranslated regions and fewer microRNA target sites. *Science* **320**, 1643–1647 (2008).
17. C. H. Jan, R. C. Friedman, J. G. Ruby, D. P. Bartel, Formation, regulation and evolution of Caenorhabditis elegans 3′UTRs. *Nature* **469**, 97–101 (2011).
18. A. Derti, P. Garrett-Engele, K. D. MacIsaac, R. C. Stevens, S. Sriram, R. Chen, C. A. Rohl, J. M. Johnson, T. Babak, A quantitative atlas of polyadenylation in five mammals. *Genome Res.* **22**, 1173–1183 (2012).
19. C. Mayr, D. P. Bartel, Widespread shortening of 3′UTRs by alternative cleavage and polyadenylation activates oncogenes in cancer cells. *Cell* **138**, 673–684 (2009).
20. Z. Xia, L. A. Donehower, T. A. Cooper, J. R. Neilson, D. A. Wheeler, E. J. Wagner, W. Li, Dynamic analyses of alternative polyadenylation from RNA-seq reveal a 3′-UTR landscape across seven tumour types. *Nat. Commun.* **5**, 5274 (2014).
21. R. Elkon, J. Drost, G. van Haaften, M. Jenal, M. Schrier, J. A. F. Oude Vrielink, R. Agami, E2F mediates enhanced alternative polyadenylation in proliferation. *Genome Biol.* **13**, R59 (2012).
22. A. J. Perrin, M. Gunda, B. Yu, K. Yen, S. Ito, S. Forster, H. A. Tissenbaum, W. B. Derry, Noncanonical control of *C. elegans* germline apoptosis by the insulin/IGF-1 and Ras/MAPK signaling pathways. *Cell Death Differ.* **20**, 97–107 (2013).
23. M. Han, P. W. Sternberg, let-60, a gene that specifies cell fates during *C. elegans* vulval induction, encodes a ras protein. *Cell* **63**, 921–931 (1990).
24. G. Battu, E. F. Hoier, A. Hajnal, The *C. elegans* G-protein-coupled receptor SRA-13 inhibits RAS/MAPK signalling during olfaction and vulval development. *Development* **130**, 2567–2577 (2003).
25. S. J. Honnen, C. Büchter, V. Schröder, M. Hoffmann, Y. Kohara, A. Kampkötter, O. Bossinger, *C. elegans* VANG-1 modulates life span via insulin/IGF-1-Like signaling. *PLOS ONE* **7**, e32183 (2012).
26. E. Schuster, J. J. M. Elwee, J. M. A. Tullet, R. Doonan, F. Matthijssens, J. S. Reece-Hoyes, I. A. Hope, J. R. Vanfleteren, J. M. Thornton, D. Gems, DamID in *C. elegans* reveals longevity-associated targets of DAF-16/FoxO. *Mol. Syst. Biol.* **6**, 399 (2010).
27. S. Ookuma, M. Fukuda, E. Nishida, Identification of a DAF-16 transcriptional target gene, scl-1, that regulates longevity and stress resistance in Caenorhabditis elegans. *Curr. Biol.* **13**, 427–431 (2003).
28. C. T. Murphy, S. A. McCarroll, C. I. Bargmann, A. Fraser, R. S. Kamath, J. Ahringer, H. Li, C. Kenyon, Genes that act downstream of DAF-16 to influence the lifespan of Caenorhabditis elegans. *Nature* **424**, 277–283 (2003).
29. S. W. Oh, A. Mukhopadhyay, B. L. Dixit, T. Raha, M. R. Green, H. A. Tissenbaum, Identification of direct DAF-16 targets controlling longevity, metabolism and diapause by chromatin immunoprecipitation. *Nat. Genet.* **38**, 251–257 (2006).
30. J. Pinkston-Gosse, C. Kenyon, DAF-16/FOXO targets genes that regulate tumor growth in Caenorhabditis elegans. *Nat. Genet.* **39**, 1403–1409 (2007).
31. J. McElwee, K. Bubb, J. H. Thomas, Transcriptional outputs of the Caenorhabditis elegans forkhead protein DAF-16. *Aging Cell* **2**, 111–121 (2003).
32. T. Kubo, T. Wada, Y. Yamaguchi, A. Shimizu, H. Handa, Knock-down of 25 kDa subunit of cleavage factor Im in Hela cells alters alternative polyadenylation within 3′-UTRs. *Nucleic Acids Res.* **34**, 6264–6271 (2006).
33. C. P. Masamha, Z. Xia, J. Yang, T. R. Albrecht, M. Li, A.-B. Shyu, W. Li, E. J. Wagner, CFIm25 links alternative polyadenylation to glioblastoma tumour suppression. *Nature* **510**, 412–416 (2014).
34. S. Lianoglou, V. Garg, J. L. Yang, C. S. Leslie, C. Mayr, Ubiquitously transcribed genes use alternative polyadenylation to achieve tissue-specific expression. *Genes Dev.* **27**, 2380–2396 (2013).
35. Y. Chu, N. Elrod, C. Wang, L. Li, T. Chen, A. Routh, Z. Xia, W. Li, E. J. Wagner, P. Ji, Nudt21 regulates the alternative polyadenylation of Pak1 and is predictive in the prognosis of glioblastoma patients. *Oncogene* **38**, 4154–4168 (2019).
36. S. Shirasawa, M. Furuse, N. Yokoyama, T. Sasazuki, Altered growth of human colon cancer cell lines disrupted at activated Ki-ras. *Science* **260**, 85–88 (1993).
37. T. E. Gillies, M. Pargett, J. M. Silva, C. K. Teragawa, F. M. Cormick, J. G. Albeck, Oncogenic mutant RAS signaling activity is rescaled by the ERK/MAPK pathway. *Mol. Syst. Biol.* **16**, e9518 (2020).
38. A. Dongre, R. A. Weinberg, New insights into the mechanisms of epithelial–mesenchymal transition and implications for cancer. *Nat. Rev. Mol. Cell Biol.* **20**, 69–84 (2019).
39. R. Di Micco, M. Fumagalli, A. Cicalese, S. Piccinin, P. Gasparini, C. Luise, C. Schurra, M. Garre', P. G. Nuciforo, A. Bensimon, R. Maestro, P. G. Pelicci, F. d'Adda di Fagagna, Oncogene-induced senescence is a DNA damage response triggered by DNA hyper-replication. *Nature* **444**, 638–642 (2006).
40. E. L. Deer, J. González-Hernández, J. D. Coursen, J. E. Shea, J. Ngatia, C. L. Scaife, M. A. Firpo, S. J. Mulvihill, Phenotype and genotype of pancreatic cancer cell lines. *Pancreas* **39**, 425–435 (2010).
41. K. C. H. Ha, B. J. Blencowe, Q. Morris, QAPA: A new method for the systematic analysis of alternative polyadenylation from RNA-seq data. *Genome Biol.* **19**, 45 (2018).

42. P. J. Sarvaiya, D. Guo, I. Ulasov, P. Gabikian, M. S. Lesniak, Chemokines in tumor progression and metastasis. *Oncotarget* **4**, 2171–2185 (2013).
43. W. Kim, R. S. Underwood, I. Greenwald, D. D. Shaye, Ortholist 2: A new comparative genomic analysis of human and *caenorhabditis elegans* genes. *Genetics* **210**, 445–461 (2018).
44. C. M. Wernicke, G. H. S. Richter, B. C. Beinvogl, S. Plehm, A. M. Schlitter, O. R. Bandapalli, O. Prazeres da Costa, U. E. Hattenhorst, I. Volkmer, M. S. Staege, I. Esposito, S. Burdach, T. G. P. Grunewald, MondoA is highly overexpressed in acute lymphoblastic leukemia cells and modulates their metabolism, differentiation and survival. *Leuk. Res.* **36**, 1185–1192 (2012).
45. D. X. He, X. T. Gu, Y. R. Li, L. Jiang, J. Jin, X. Ma, Methylation-regulated miR-149 modulates chemoresistance by targeting GlcNAcN-deacetylase/N-sulfotransferase-1 in human breast cancer. *FEBS J.* **281**, 4718–4730 (2014).
46. A. Tivnan, Z. Zakaria, C. Ã.. O'Leary, D. Kögel, J. L. Pokorny, J. N. Sarkaria, J. H. M. Prehn, Inhibition of multidrug resistance protein 1 (MRP1) improves chemotherapy drug response in primary and recurrent glioblastoma multiforme. *Front. Neurosci.* **9**, (2015).
47. C. Thivierge, H. W. Tseng, V. K. Mayya, C. Lussier, S. P. Gravel, T. F. Duchaine, Alternative polyadenylation confers *Pten* mRNAs stability and resistance to microRNAs. *Nucleic Acids Res.* **46**, 10340–10352 (2018).
48. C. Scheel, E. N. Eaton, S. H. J. Li, C. L. Chaffer, F. Reinhardt, K. J. Kah, G. Bell, W. Guo, J. Rubin, A. L. Richardson, R. A. Weinberg, Paracrine and autocrine signals induce and maintain mesenchymal and stem cell states in the breast. *Cell* **145**, 926–940 (2011).
49. M. Gao, L. Miao, M. Liu, C. Li, C. Yu, H. Yan, Y. Yin, Y. Wang, X. Qi, J. Ren, MiR-145 sensitizes breast cancer to doxorubicin by targeting multidrug resistance-associated protein-1. *Oncotarget* **7**, 59714–59726 (2016).
50. B. L. Parsons, K. L. McKim, M. B. Myers, Variation in organ-specific *PIK3CA* and *KRAS* mutant levels in normal human tissues correlates with mutation prevalence in corresponding carcinomas. *Environ. Mol. Mutagen.* **58**, 466–476 (2017).
51. S. Mueller, T. Engleitner, R. Maresch, M. Zukowska, S. Lange, T. Kaltenbacher, B. Konukiewitz, R. Öllinger, M. Zwiebel, A. Strong, H. Y. Yen, R. Banerjee, S. Louzada, B. Fu, B. Seidler, J. Götzfried, K. Schuck, Z. Hassan, A. Arbeiter, N. Schönhuber, S. Klein, C. Veltkamp, M. Friedrich, L. Rad, M. Barenboim, C. Ziegenhain, J. Hess, O. M. Dovey, S. Eser, S. Parekh, F. Constantino-Casas, J. de la Rosa, M. I. Sierra, M. Fraga, J. Mayerle, G. Klöppel, J. Cadiñanos, P. Liu, G. Vassiliou, W. Weichert, K. Steiger, W. Enard, R. M. Schmid, F. Yang, K. Unger, G. Schneider, I. Varela, A. Bradley, D. Saur, R. Rad, Evolutionary routes and KRAS dosage define pancreatic cancer phenotypes. *Nature* **554**, 62–68 (2018).
52. M. S. Anglesio, N. Papadopoulos, A. Ayhan, T. M. Nazeran, M. Noë, H. M. Horlings, A. Lum, S. Jones, J. Senz, T. Seckin, J. Ho, R. C. Wu, V. Lac, H. Ogawa, B. Tessier-Cloutier, R. Alhassan, A. Wang, Y. Wang, J. D. Cohen, F. Wong, A. Hasanovic, N. Orr, M. Zhang, M. Popoli, W. McMahon, L. D. Wood, A. Mattox, C. Allaire, J. Segars, C. Williams, C. Tomasetti, N. Boyd, K. W. Kinzler, C. B. Gilks, L. Diaz, T. L. Wang, B. Vogelstein, P. J. Yong, D. G. Huntsman, I. M. Shih, Cancer-associated mutations in endometriosis without cancer. *N. Engl. J. Med.* **376**, 1835–1848 (2017).
53. Y. Wang, Y. Xu, W. Yan, P. Han, J. Liu, J. Gong, D. Li, X. Ding, H. Wang, Z. Lin, D. Tian, J. Liao, CFIm25 inhibits hepatocellular carcinoma metastasis by suppressing the p38 and JNK/c-Jun signaling pathways. *Oncotarget* **9**, 11783–11793 (2018).
54. S. Tan, H. Li, W. Zhang, Y. Shao, Y. Liu, H. Guan, J. Wu, Y. Kang, J. Zhao, Q. Yu, Y. Gu, K. Ding, M. Zhang, W. Qian, Y. Zhu, H. Cai, C. Chen, P. E. Lobie, X. Zhao, J. Sun, T. Zhu, NUDT21 negatively regulates PSMB2 and CXXC5 by alternative polyadenylation and contributes to hepatocellular carcinoma suppression. *Oncogene* **37**, 4887–4900 (2018).
55. J. C. Lou, Y. L. Lan, J. X. Gao, B. B. Ma, T. Yang, Z. B. Yuan, H. Q. Zhang, T. Z. Zhu, N. Pan, S. Leng, G. J. Song, B. Zhang, Silencing NUDT21 attenuates the mesenchymal identity of glioblastoma cells via the NF-κB pathway. *Front. Mol. Neurosci.* **10**, (2017).
56. S. P. Cole, K. E. Sparks, K. Fraser, D. W. Loe, C. E. Grant, G. M. Wilson, R. G. Deeley, Pharmacological characterization of multidrug resistant MRP-transfected human tumor cells. *Cancer Res.* **54**, 5902–5910 (1994).
57. A. Yamada, M. Nagahashi, T. Aoyagi, W. C. Huang, S. Lima, N. C. Hait, A. Maiti, K. Kida, K. P. Terracina, H. Miyazaki, T. Ishikawa, I. Endo, M. R. Waters, Q. Qi, L. Yan, S. Milstien, S. Spiegel, K. Takabe, ABCC1-exported sphingosine-1-phosphate, produced by sphingosine kinase 1, shortens survival of mice and patients with breast cancer. *Mol. Cancer Res.* **16**, 1059–1070 (2018).
58. S. H. Lee, I. Singh, S. Tisdale, O. Abdel-Wahab, C. S. Leslie, C. Mayr, Widespread intronic polyadenylation inactivates tumour suppressor genes in leukaemia. *Nature* **561**, 127–131 (2018).
59. T. J. Pugh, O. Morozova, E. F. Attiyeh, S. Asgharzadeh, J. S. Wei, D. Auclair, S. L. Carter, K. Cibulskis, M. Hanna, A. Kiezun, J. Kim, M. S. Lawrence, L. Lichenstein, A. McKenna, C. S. Pedamallu, A. H. Ramos, E. Shefler, A. Sivachenko, C. Sougnez, C. Stewart, A. Ally, I. Birol, R. Chiu, R. D. Corbett, M. Hirst, S. D. Jackman, B. Kamoh, A. H. Khodabakshi, M. Krzywinski, A. Lo, R. A. Moore, K. L. Mungall, J. Qian, A. Tam, N. Thiessen, Y. Zhao, K. A. Cole, M. Diamond, S. J. Diskin, Y. P. Mosse, A. C. Wood, L. Ji, R. Sposto, T. Badgett, W. B. London, Y. Moyer, J. M. Gastier-Foster, M. A. Smith, J. M. G. Auvil, D. S. Gerhard, M. D. Hogarty, S. J. M. Jones, E. S. Lander, S. B. Gabriel, G. Getz, R. C. Seeger, J. Khan, M. A. Marra, M. Meyerson, J. M. Maris, The genetic landscape of high-risk neuroblastoma. *Nat. Genet.* **45**, 279–284 (2013).
60. D. J. Dickinson, A. M. Pani, J. K. Heppert, C. D. Higgins, B. Goldstein, Streamlined genome engineering with a self-excising drug selection cassette. *Genetics* **200**, 1035–1049 (2015).
61. L. Collado-Torres, A. Nellore, A. C. Frazee, C. Wilks, M. I. Love, B. Langmead, R. A. Irizarry, J. T. Leek, A. E. Jaffe, Flexible expressed region analysis for RNA-seq with derfinder. *Nucleic Acids Res.* **45**, e9 (2017).
62. S. Anders, A. Reyes, W. Huber, Detecting differential usage of exons from RNA-seq data. *Genome Res.* **22**, 2008–2017 (2012).
63. M. I. Love, W. Huber, S. Anders, Moderated estimation of fold change and dispersion for RNA-seq data with DESeq2. *Genome Biol.* **15**, 550 (2014).
64. J. Harrow, A. Frankish, J. M. Gonzalez, E. Tapanari, M. Diekhans, F. Kokocinski, B. L. Aken, D. Barrell, A. Zadissa, S. Searle, I. Barnes, A. Bignell, V. Boychenko, T. Hunt, M. Kay, G. Mukherjee, J. Rajan, G. Despacio-Reyes, G. Saunders, C. Steward, R. Harte, M. Lin, C. Howald, A. Tanzer, T. Derrien, J. Chrast, N. Walters, S. Balasubramanian, B. Pei, M. Tress, J. M. Rodriguez, I. Ezkurdia, J. van Baren, M. Brent, D. Haussler, M. Kellis, A. Valencia, A. Reymond, M. Gerstein, R. Guigo, T. J. Hubbard, GENCODE: The reference human genome annotation for the ENCODE project. *Genome Res.* **22**, 1760–1774 (2012).
65. R. Patro, S. M. Mount, C. Kingsford, Sailfish enables alignment-free isoform quantification from RNA-seq reads using lightweight algorithms. *Nat. Biotechnol.* **32**, 462–464 (2014).
66. Y. Sun, J. Campisi, C. Higano, T. M. Beer, P. Porter, I. Coleman, L. True, P. S. Nelson, Treatment-induced damage to the tumor microenvironment promotes prostate cancer therapy resistance through WNT16B. *Nat. Med.* **18**, 1359–1368 (2012).
67. B. Bierie, S. E. Pierce, C. Kroeger, D. G. Stover, D. R. Pattabiraman, P. Thiru, J. L. Donaher, F. Reinhardt, C. L. Chaffer, Z. Keckesova, R. A. Weinberg, Integrin-β4 identifies cancer stem cell-enriched populations of partially mesenchymal carcinoma cells. 114, E2337 (E2346, 2017).
68. X. Li, P. D. Stevens, H. Yang, P. Gulhati, W. Wang, B. M. Evers, T. Gao, The deubiquitination enzyme USP46 functions as a tumor suppressor by controlling PHLPP-dependent attenuation of Akt signaling in colon cancer. *Oncogene* **32**, 471–478 (2013).
69. E. F. Wagner, Á. R. Nebreda, Signal integration by JNK and p38 MAPK pathways in cancer development. *Nat. Rev. Cancer* **9**, 537–549 (2009).
70. D. Luo, D. Liu, W. Shi, H. Jiang, W. Liu, X. Zhang, Y. Bao, W. Yang, X. Wang, C. Zhang, H. Wang, L. Yuan, Y. Chen, T. Qu, D. Ou, W. Shen, S. Yang, PPA1 promotes NSCLC progression via a JNK- and TP53-dependent manner. *Oncogenesis* **8**, 53 (2019).
71. D. Subramani, S. K. Alahari, Integrin-mediated function of Rab GTPases in cancer progression. *Mol. Cancer* **9**, 312 (2010).
72. A. M. Tari, M. C. Hung, K. Li, G. Lopez-Berestein, Growth inhibition of breast cancer cells by Grb2 downregulation is correlated with inactivation of mitogen-activated protein kinase in EGFR, but not in ErbB2, cells. *Oncogene* **18**, 1325–1332 (1999).
73. H. Y. Chow, B. Dong, C. A. Valencia, C. T. Zeng, J. N. Koch, T. Y. Prudnikova, J. Chernoff, Group I Paks are essential for epithelial-mesenchymal transition in an Apc-driven model of colorectal cancer. *Nat. Commun.* **9**, 3473 (2018).

Acknowledgments: We thank D. Kaplan and S. Egan for critical reading of the manuscript and suggestions. We thank S. Freeman, K. Lau, and P. Paroutis for assistance and suggestions regarding microscopy and image analysis. We thank the Donnelly Sequencing Centre at the University of Toronto for performing the RNA-seq. **Funding:** This work was supported by operating grants from the Canadian Institutes for Health Research to W.B.D. and M.D. (PJT-155928, 2018/4-2023/3), a Genome Canada Disruptive Innovations in Technology Grant to M.D.W. (2016/7-2018/6), and a Natural Sciences and Engineering Research Council of Canada grant (RGPIN-2019-07014) to M.D.W. W.B.D. is supported by the Canada Research Chair Program and is Vice Chair of Fundamental Research in the Garron Family Cancer Centre at the Hospital for Sick Children. M.D.W. is supported by the Canada Research Chairs Program and an Early Researcher Award from the Ontario Ministry of Research and Innovation. K.E.Y. was supported by a SickKids Restracomp Fellowship (2017/1-2019/1). A.Sa. was supported by a SickKids Restracomp Fellowship (2021/01-2021/09) and CIHR CGS Graduate Scholarship (2019/09-2020/12). J.E. is funded by the Canadian Institutes for Health Research (PJT-148746, 2016-2020). **Author contributions:** Conceptualization: A.Su., M.H., and W.B.D. Methodology: A.Su., M.H., H.H., M.M., and K.E.Y. Investigation: A.Su., M.H., H.H., M.M., B.Y., H.N., A.Sa., B.L., and B.Z. Supervision: W.B.D., M.D.W., J.E., and M.D. Writing—original draft: A.Su. and W.B.D. Writing—review and editing: A.Su., J.E., M.D.W., M.D., and W.B.D. **Competing interests:** The authors declare that they have no competing interests. **Data and materials availability:** All data needed to evaluate the conclusions in the paper are present in the paper and/or the Supplementary Materials. Raw sequencing datasets generated in the current study are available through ArrayExpress under accession IDs E-MTAB-9147 (*C. elegans*) and E-MTAB-9207 (*H. sapiens*). The data and scripts used to reproduce the analyses and figures related to the *C. elegans* and human RNA-seq experiments can be found at https://zenodo.org/record/5495741.

Submitted 17 February 2021
Accepted 29 October 2021
Published 17 December 2021
10.1126/sciadv.abh0562